






Truncated partial-wave analysis for η -photoproduction observables via Bayesian statistics

Philipp Kroenert , Yannick Wunderlich , Farah Afzal , and Annika Thiel 
Helmholtz Institut für Strahlen- und Kernphysik, Universität Bonn, D-53115 Bonn, Germany

 (Received 18 May 2023; revised 15 November 2023; accepted 6 February 2024; published 10 April 2024)

A truncated partial-wave analysis is performed for η photoproduction off the proton using the polarization observables σ_0 , Σ , T , E , F , and G . Through this approach, model-independent estimates of the electromagnetic multipole parameters are calculated. Based on these estimates, predictions are made for polarization observables that have not yet been measured. These predictions identify promising future measurements that could resolve the inherent mathematical ambiguities within the results. Bayesian inference is combined for the first time with truncated partial-wave analysis, analyzing different truncation orders for six energy bins near the ηp -production threshold, i.e., $E_\gamma^{\text{lab}} \in [750, 1250]$ MeV.

DOI: [10.1103/PhysRevC.109.045206](https://doi.org/10.1103/PhysRevC.109.045206)

I. INTRODUCTION

Baryon spectroscopy is an experimental technique to acquire a better understanding of the strong interaction and its fundamental theoretical description given by quantum chromodynamics. Particles (for example, pions, real photons, as well as electrons [1]) are brought to collision with a nucleon. With a sufficiently high center-of-mass energy, the nucleon can be excited to a resonant state, which is classified as a distinct particle with certain intrinsic properties. Two well-established examples for baryon resonances are the delta resonance $\Delta(1232)3/2^+$ and the Roper resonance $N(1440)1/2^+$ [2]. As such resonances are often formed and decay via the strong interaction, their proper lifetimes are rather short; for the above examples, on the order of 10^{-24} s. A direct detection of resonances with state-of-the-art detectors is not possible. Instead, the analysis of the final-state particles angular distributions using partial-wave analysis (PWA), allows us to draw conclusions about the formation of the resonance and its inherent properties such as total angular momentum, mass, decay width, and parity. Up to the present day, single pseudoscalar meson photoproduction reactions are the experimentally most studied reactions in terms of baryon spectroscopy. A comprehensive overview can be found in the recently published review on light baryon spectroscopy by Thiel *et al.* [1]. The experimental data which are used as input to partial-wave analyses are called polarization observables. In single pseudoscalar meson photoproduction, there are sixteen linearly independent measurable quantities. Multiple facilities worldwide [3–7] have contributed to a large database. In addition, multiple PWA approaches [8–13] do exist for describing the data and extracting information about the resonant states. The results of this paper are compared with the K -matrix model of Bonn-Gatchina [9], the dynamical coupled-channel approach of Jülich-Bonn [10], and the unitarized isobar-model of Eta-MAID [11]. However, these approaches depend on an energy-dependent parametrization for the complex amplitudes [1], leading to model-dependent outcomes. For a detailed comparison of these three PWA

approaches, the reader is advised to Refs. [1,14]. Resonant states can also be predicted in a purely mathematical manner via theory models based on quantum chromodynamics, such as quark models or lattice quantum chromodynamics; see, for example, Ref. [15]. However, theory models predicted significantly more states than are experimentally confirmed, predominantly in the higher-mass region, which is known as the missing-resonance problem [1]. This unsolved issue motivates further studies and the exploration of new approaches within this field of physics. In this paper, a completely model-independent analysis approach, namely, truncated partial-wave analysis (TPWA) [16–20], is employed. This avoids the bias present in other PWA approaches. In general, PWA as well as TPWA may exhibit mathematical ambiguities in their results, indicating that various solutions can effectively describe the same data points. These ambiguities arise from the intrinsic mathematical nature of the problem. As such, it is an essential step in any analysis using experimental data to check for potential ambiguities and evaluate their significance in comparison to each other. Mathematical ambiguities in TPWA were first investigated by Omelaenko [21]. A detailed treatment of the subject can be found in Refs. [18–20]. The application of TPWA to experimental data (π^0 photoproduction off the proton for the first- and second-resonance region) was conducted in detail by Wunderlich [19] using the maximum likelihood method. Among other things, the effect of measurement uncertainties on ambiguities was investigated. This paper is the first to perform a TPWA using Bayesian inference. Therefore, the results in this paper are given as distributions, as opposed to point estimates in previous PWA and TPWA approaches, allowing the uncertainty of an estimated parameter to be quantified with an unprecedented level of detail, which is of particular importance. Through this approach it becomes possible to study the phase space in more detail and, by association, the structure of the above-mentioned ambiguities. It is even possible to discover a certain connectivity between

different solutions, indicating problematic ambiguities. The results of this paper comprises the estimation of complex electromagnetic multipole parameters for various maximal angular momenta ℓ_{\max} . Based on these estimations, for the first time, model-independent predictions for unmeasured polarization observables are computed.

This paper is structured as follows: a concise introduction to Bayesian statistics is given in Sec. II. An outline of TPWA, hence the foundation of the employed model, is provided in Sec. III, followed by a discussion of the mathematical ambiguities. The employed datasets are introduced and discussed in Sec. IV, accompanied by the discussion of their systematic uncertainties and correlations between the data points used. Within Sec. V the posterior distribution, centerpiece of the analyses, is introduced. Finally, the results of TPWA examined via Bayesian inference are presented in Sec. VI.

II. BASICS OF BAYESIAN STATISTICS

The fundamental equation of Bayesian statistics is Bayes' theorem [22,23]:

$$p(\Theta | \mathbf{y}) = \frac{p(\mathbf{y} | \Theta) p(\Theta)}{\int p(\mathbf{y} | \Theta) p(\Theta) d\Theta}. \quad (1)$$

Herein, Θ denotes the parameters of the model used whereas \mathbf{y} stands for the employed data.

The posterior distribution $p(\Theta | \mathbf{y})$ is in general a multi-dimensional probability distribution reflecting the probability of the model given the data. It consists of the likelihood distribution $p(\mathbf{y} | \Theta)$, comprising the data points and model predictions, and the prior distribution $p(\Theta)$, which inhibits the current knowledge about the parameters of the model, before the data are taken into consideration. The denominator in Eq. (1) plays the role of a normalization factor and can be neglected within the computations of parameter estimation as it is constant for fixed \mathbf{y} . The definitions for the likelihood distribution and prior distributions employed in this paper can be found in Secs. V A and V B.

The overall goal of each analysis is to scan the relevant regions of the posterior accurately. From this, the parameter distributions can then be extracted, i.e., their marginal distributions.¹ In general, the posterior is nontrivial and the integrals encountered in the derivation of the marginal distributions cannot be solved analytically. Instead, one can employ numerical methods, such as Markov chain Monte Carlo (MCMC) algorithms, in order to estimate the involved integrals. For instance, the Metropolis-Hastings [24,25] or the Hamiltonian Monte Carlo [26,27] algorithm can be used, of which the latter one is applied in this work. The convergence of the Markov chains² can be monitored by convergence

¹The marginal distribution of Θ_1 with respect to the posterior distribution $p(\Theta_1, \Theta_2 | \mathbf{y})$ is defined as $p(\Theta_1 | \mathbf{y}) = \int d\Theta_2 p(\Theta_1, \Theta_2 | \mathbf{y})$ [23].

²“A sequence X_1, X_2, \dots of random elements of some set is a Markov chain if the conditional distribution of X_{n+1} given X_1, \dots, X_n depends on X_n only” [[28], p. 2].

diagnostics such as the potential-scale-reduction statistic \hat{R} [29], Monte Carlo standard error [28] (which depends on the effective sample size [23]), and trace plots [30].

To check the plausibility of the model under consideration, a posterior predictive check can be performed [23]. Herein, replicated data distributions \mathbf{y}^{rep} are generated using the sampled parameter distributions as input for the posterior distribution, while at the same time treating the data points as unknown parameters. In contrast with maximum likelihood or maximum *a posteriori* estimation, the marginal parameter estimates of Bayesian inference are given as distributions. This allows us to quantify the uncertainty of a parameter with an unmatched level of detail. In addition, point estimates and the marginal parameter estimates of Bayesian inference differ in their underlying interpretation, making the latter an intriguing additional analysis approach.

III. TRUNCATED PARTIAL-WAVE ANALYSIS

Within this section, the basic equations of TPWA for single pseudoscalar-meson photoproduction are outlined. For an in-depth explanation, the reader is advised to Refs. [19,20].

Polarization observables are the measurable quantities of interest in single pseudoscalar-meson photoproduction. They are used as experimental input for a TPWA. In total there are sixteen polarization observables, which can be calculated by measuring differential cross sections under different polarization states. Three groups can be distinguished: the unpolarized differential cross section, three single-polarization observables, and twelve double-polarization observables [31]. A comprehensive list of the required polarization states for each observable is given in Table I while a mathematical definition is given in Table II.

The theoretical prediction of a profile function³ of a polarization observable depends on the energy W as well as the scattering angle θ in the center-of-mass frame. It can be expressed as an expansion into the basis of associated Legendre polynomials $P_k^{\beta_\alpha}$ [20]:

$$\tilde{\Omega}_{\text{theo}}^\alpha(W, \theta) = \rho \sum_{k=\beta_\alpha}^{2\ell_{\max} + \beta_\alpha + \gamma_\alpha} \mathcal{A}_k^\alpha(W) P_k^{\beta_\alpha}(\cos \theta). \quad (2)$$

Equation (2) includes a kinematic phase-space factor ρ , angular expansion parameters $\beta_\alpha, \gamma_\alpha$, which are fixed parameters for each of the sixteen polarization observables of pseudoscalar-meson photoproduction, and energy-dependent series coefficients \mathcal{A}_k^α :

$$\mathcal{A}_k^\alpha(W) = \mathcal{M}^\dagger(W) \mathcal{C}_k^\alpha \mathcal{M}(W). \quad (3)$$

Here, \mathcal{M} denotes the complex multipole vector, which contains all participating multipoles involved for the truncation order ℓ_{\max} . A valid choice for the definition of this vector, by

³The profile function $\tilde{\Omega}^\alpha(W, \theta)$ of an observable $\Omega^\alpha(W, \theta)$ is defined as $\tilde{\Omega}^\alpha(W, \theta) := \sigma_0(W, \theta) \Omega^\alpha(W, \theta)$, where σ_0 is the unpolarized differential cross section.

TABLE I. This table collects the polarization configurations (beam, target, recoil) which allow us to measure the sixteen polarization observables of pseudoscalar meson photoproduction. In the center-of-mass coordinate system, the unprimed coordinates are chosen as follows: \hat{z} axis along incident photon beam direction and \hat{y} perpendicular to the reaction plane \hat{x} - \hat{z} . The primed coordinates is a rotation of the unprimed coordinates such that the final-state meson momentum points along the \hat{z}' axis. The table is redrawn from Ref. [31]. A mathematical definition of the observables can be found in Table II.

Observable	Beam polarization	Direction of target- or recoil-nucleon polarization
σ_0	Unpolarized	
Σ	Linear	
T	Unpolarized	y
P	Unpolarized	y'
H	Linear	x
P	Linear	y
G	Linear	z
F	Circular	x
E	Circular	z
$O_{x'}$	Linear	x'
T	Linear	y'
$O_{z'}$	Linear	z'
$C_{x'}$	Circular	x'
$C_{z'}$	Circular	z'
$T_{x'}$	Unpolarized	x, x'
$L_{x'}$	Unpolarized	z, x'
Σ	Unpolarized	y, y'
$T_{z'}$	Unpolarized	x, z'
$L_{z'}$	Unpolarized	z, z'

TABLE II. The definition of the sixteen polarization observables in terms of transversity amplitudes b_i are displayed. The table is adapted from Ref. [33]. The definition of the observables in terms of the required polarization configurations can be found in Table I.

Observable	Transversity representation (ρ)	Type
$\check{\Omega}^1 = \sigma_0$	$\frac{1}{2}(b_1 ^2 + b_2 ^2 + b_3 ^2 + b_4 ^2)$	\mathcal{S}
$\check{\Omega}^4 = -\check{\Sigma}$	$\frac{1}{2}(b_1 ^2 + b_2 ^2 - b_3 ^2 - b_4 ^2)$	
$\check{\Omega}^{10} = -\check{T}$	$\frac{1}{2}(- b_1 ^2 + b_2 ^2 + b_3 ^2 - b_4 ^2)$	
$\check{\Omega}^{12} = \check{P}$	$\frac{1}{2}(- b_1 ^2 + b_2 ^2 - b_3 ^2 + b_4 ^2)$	
$\check{\Omega}^3 = \check{G}$	$\text{Im}[-b_1 b_3^* - b_2 b_4^*]$	\mathcal{BT}
$\check{\Omega}^5 = \check{H}$	$\text{Re}[b_1 b_3^* - b_2 b_4^*]$	
$\check{\Omega}^9 = -\check{E}$	$\text{Re}[b_1 b_3^* + b_2 b_4^*]$	
$\check{\Omega}^{11} = \check{F}$	$\text{Im}[b_1 b_3^* - b_2 b_4^*]$	
$\check{\Omega}^{14} = \check{O}_{x'}$	$\text{Re}[-b_1 b_4^* + b_2 b_3^*]$	\mathcal{BR}
$\check{\Omega}^7 = -\check{O}_{z'}$	$\text{Im}[-b_1 b_4^* - b_2 b_3^*]$	
$\check{\Omega}^{16} = -\check{C}_{x'}$	$\text{Im}[b_1 b_4^* - b_2 b_3^*]$	
$\check{\Omega}^2 = -\check{C}_{z'}$	$\text{Re}[b_1 b_4^* + b_2 b_3^*]$	
$\check{\Omega}^6 = -\check{T}_{x'}$	$\text{Re}[-b_1 b_2^* + b_3 b_4^*]$	\mathcal{TR}
$\check{\Omega}^{13} = -\check{T}_{z'}$	$\text{Im}[b_1 b_2^* - b_3 b_4^*]$	
$\check{\Omega}^8 = \check{L}_{x'}$	$\text{Im}[-b_1 b_2^* - b_3 b_4^*]$	
$\check{\Omega}^{15} = \check{L}_{z'}$	$\text{Re}[-b_1 b_2^* - b_3 b_4^*]$	

means of electromagnetic multipoles [32], is

$$\mathcal{M}(W) = [E_{0+}(W), E_{1+}(W), M_{1+}(W), M_{1-}(W), \\ \times E_{2+}(W), E_{2-}(W), M_{2+}(W), M_{2-}(W), \dots, \\ \times E_{\ell_{\max}+}(W), E_{\ell_{\max}-}(W), M_{\ell_{\max}+}(W), M_{\ell_{\max}-}(W)]. \quad (4)$$

In addition, Eq. (3) contains a complex $4\ell_{\max} \times 4\ell_{\max}$ matrix \mathcal{C} for each observable α and each summand k . Its general definition can be found in Ref. [19].⁴ From these matrices one can not only read off the contributing partial waves but also their interferences with each other [20].

Equations (2) to (4) imply the following:

- (1) The statistical analysis is performed for a single energy at a time.
- (2) The polarization observable $\Omega^\alpha(W, \theta)$ and the unpolarized differential cross section $\sigma_0(W, \theta)$ have to share the same energy and angular binning.
- (3) The observables $\Omega^\alpha(W, \theta)$ used within the TPWA have to share the same energy binning.
- (4) As $\check{\Omega}^\alpha(W, \theta)$ is an observable, i.e., a real number, the matrices \mathcal{C}_k^α are Hermitian.
- (5) The bilinear form of \mathcal{A}_k^α gives rise to mathematical ambiguities, as certain transformations leave this quantity invariant.

The last point is discussed in more detail in the following.

A. Ambiguities

Ambiguities in PWA or TPWA refer to situations in which multiple configurations of the model parameters can describe the data points with similar levels of accuracy. This phenomenon is apparent in the reproduced data distributions in Figs. 1 and 2 where the different colored distributions, corresponding to multiple ambiguities, nearly overlap. In the following discussion, various types of mathematical ambiguities are examined and it is concluded that only so-called accidental discrete ambiguities can appear in the results of this paper.

The origin of the immanent mathematical ambiguities lies in the definition of the polarization observables. For photoproduction, they can be written in general as a bilinear product of the form [33–35]

$$\check{\Omega}^\alpha(W, \theta) = \kappa b^\dagger(W, \theta) \Gamma^\alpha b(W, \theta), \quad (5)$$

with a numerical prefactor κ , a vector b of length N_A , containing the complex spin amplitudes b_i , and a matrix Γ^α with dimensions $N_A \times N_A$. Certain transformations T of the complex spin amplitudes $b_i(W, \theta) \xrightarrow{T} \tilde{b}_i(W, \theta)$ leave the bilinear product and thus the observable invariant. Hence, when all observables in a subset $\{\check{\Omega}^{\alpha_1}, \dots, \check{\Omega}^{\alpha_n}\}$ are invariant under the same transformation, an ambiguity emerges [19,33], as the experimental distinction between b_i and \tilde{b}_i is not possible

⁴An overall factor of 1/2 is missing in the formula for \mathcal{C}_k^α in Ref. [19].

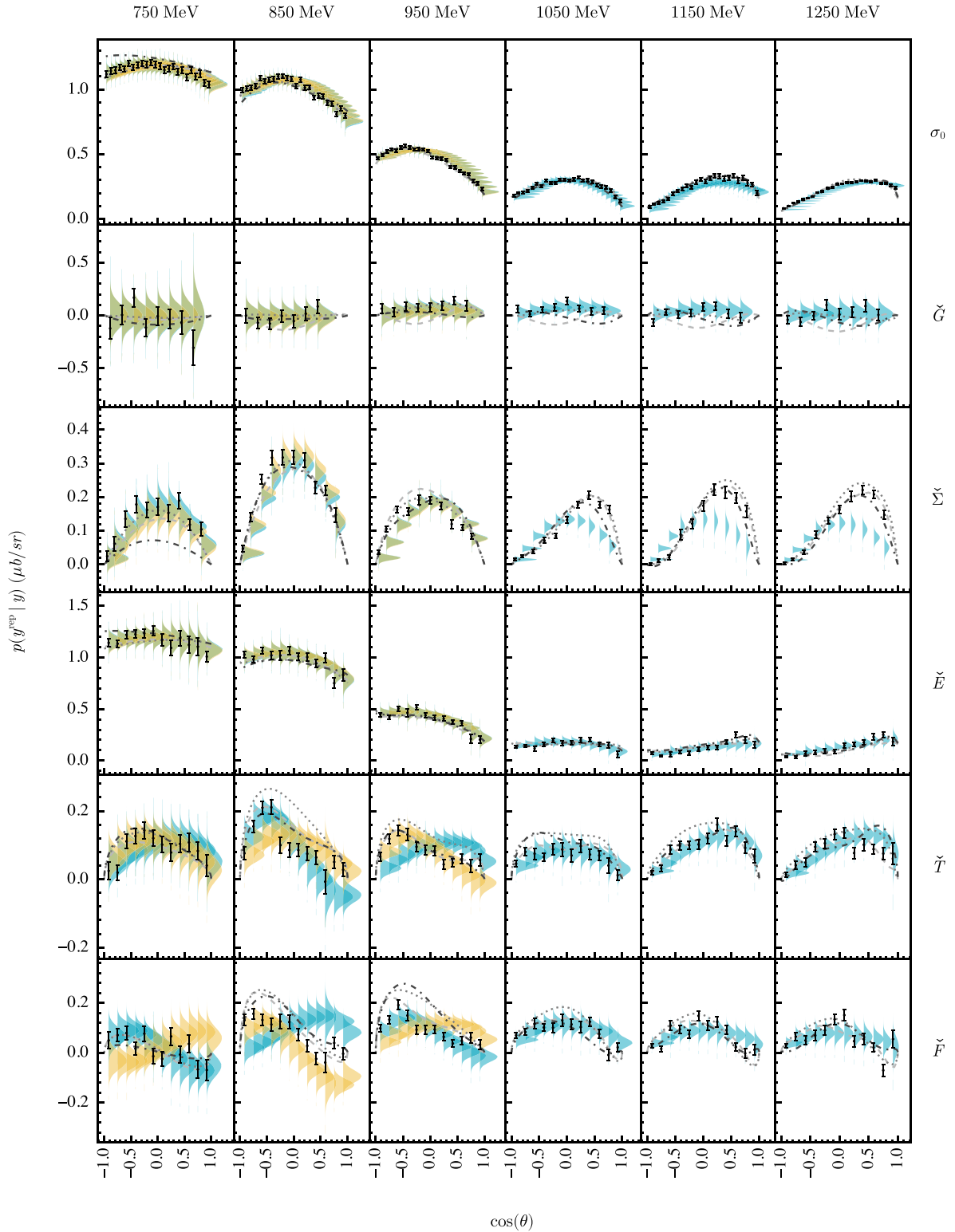


FIG. 1. Posterior predictive check for the profile functions σ_0 , \tilde{G} , $\tilde{\Sigma}$, \tilde{E} , \tilde{T} , and \tilde{F} for truncation order $\ell_{\max} = 1$ and energy bins $E_{\nu}^{\text{lab}} = [750, 850, 950, 1050, 1150, 1250]$ MeV. The reproduced data distributions for the different solutions are shown together with the original data with statistical uncertainties as black points. Each solution group is drawn in a different color and each peak of a distribution corresponds to an accidental ambiguity. In addition, the corresponding values from EtaMAID2018 [48] (dashed line), BnGa-2019 [42] (dotted line), and JüBo-2022 [47] (dash-dotted line) are shown as well.

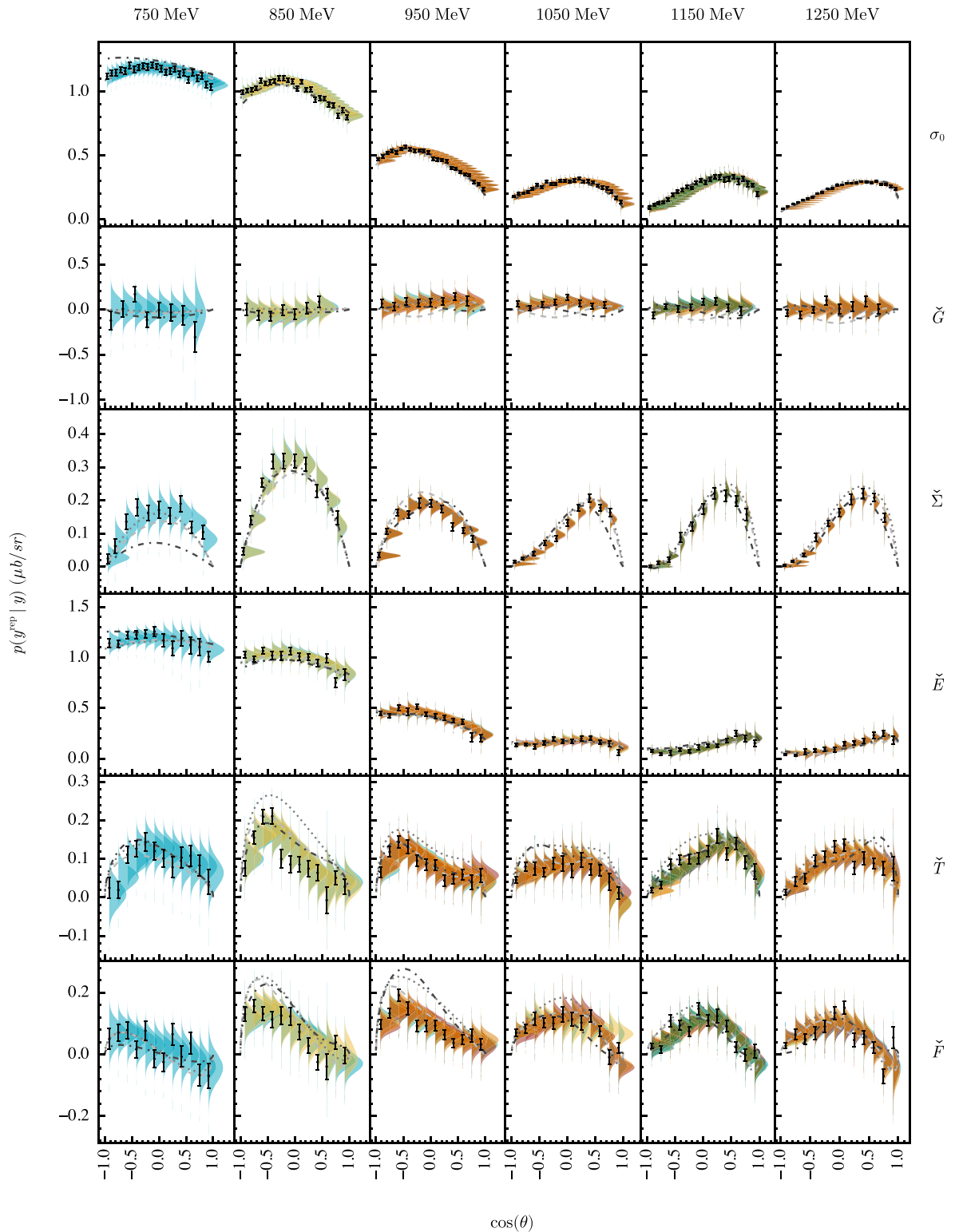


FIG. 2. Posterior predictive check for the profile functions σ_0 , \check{G} , $\check{\Sigma}$, \check{E} , \check{T} , and \check{F} for truncation order $\ell_{\max} = 2$ and energy bins $E_{\gamma}^{\text{lab}} = [750, 850, 950, 1050, 1150, 1250]$ MeV. The reproduced data distributions for the different solutions are shown together with the original data with statistical uncertainties as black points. Each solution group is drawn in a different color and each peak of a distribution corresponds to an accidental ambiguity. In addition, the corresponding values from EtaMAID2018 [48] (dashed line), BnGa-2019 [42] (dotted line), and JüBo-2022 [47] (dash-dotted line) are shown as well.

any more. Such an ambiguity can be resolved by including a further observable $\hat{\Omega}^{\alpha_i}$ into the subset, which is not invariant under the specific transformation [19,33]. There exists one special case of an ambiguity which cannot be resolved by including any further observables, namely, the simultaneous rotation of all transversity amplitudes by the same (possibly energy- and angle-dependent) phase: $b_i(W, \theta) \xrightarrow{T} e^{i\phi(W, \theta)} b_i(W, \theta)$ (see Ref. [33]). However, this continuous ambiguity can be ignored for the special case of a TPWA, since the angle-dependent part of the ambiguity is generally removed by the assumed truncation (see comments made in Ref. [36]), and the energy-dependent part is fixed by imposing certain phase conventions for the multipoles. The formalism for the remaining relevant discrete ambiguities in a TPWA is outlined briefly in the following. For more information about discrete as well as continuous ambiguities in the case of the complete experiment analysis, see the paper of Chiang and Tabakin [33].

As shown by Omelaenko [19,21], in a TPWA (truncated at some finite $\ell_{\max} \geq 1$) the complex spin-amplitudes can be expressed (up to kinematical prefactors) as a finite product of irreducible polynomials:

$$b_1(W, \theta) \propto \prod_{k=1}^{2\ell_{\max}} \left(\tan \frac{\theta}{2} + \beta_k(W) \right), \quad (6)$$

$$b_2(W, \theta) \propto \prod_{k=1}^{2\ell_{\max}} \left(\tan \frac{\theta}{2} - \beta_k(W) \right), \quad (7)$$

$$b_3(W, \theta) \propto \prod_{k=1}^{2\ell_{\max}} \left(\tan \frac{\theta}{2} + \alpha_k(W) \right), \quad (8)$$

$$b_4(W, \theta) \propto \prod_{k=1}^{2\ell_{\max}} \left(\tan \frac{\theta}{2} - \alpha_k(W) \right), \quad (9)$$

with the complex roots $\alpha_k(W)$ and $\beta_k(W)$, which are in essence equivalent to multipoles. It can be shown [18,21,37] that the special case where $\tan(\theta/2) = 0$ implies a direct connection between the roots:

$$\prod_{i=1}^{2\ell_{\max}} \alpha_i(W) = \prod_{j=1}^{2\ell_{\max}} \beta_j(W). \quad (10)$$

All transformations T which correspond to a discrete ambiguity of the four group- \mathcal{S} observables $\{\sigma_0, \check{\Sigma}, \check{T}, \check{P}\}$ must also satisfy Eq. (10), which allows us to rule out a major part of the maximal possible $4^{2\ell_{\max}}$ [18] discrete ambiguity-transformations from the beginning. The so-called ‘‘double ambiguity’’ [18,21], which corresponds to the simultaneous complex conjugation of all roots automatically preserves the constraint in Eq. (10).

Unfortunately, there can also occur so-called accidental ambiguities. These emerge when any discrete ambiguity other than the double ambiguity of all roots approximately fulfills Eq. (10) [18]. The accidental ambiguities as well as the double ambiguity can in principle be resolved by including further observables into the analysis apart from the four group \mathcal{S} observables. Candidates for observables capable of resolving

the above-mentioned discrete ambiguities would be either \check{F} , \check{G} or any of the \mathcal{BR} - and \mathcal{TR} -type observables.

The accidental ambiguities cannot be avoided for analyses of real data due to their abundance (i.e., $4^{2\ell_{\max}} - 2$ possible candidates exist for such ambiguities), and they will show up as modes within the posterior distribution and thus in the marginal parameter distributions.

In contrast with the discrete ambiguities described above, there can also exist so-called continuous ambiguities in the TPWA (in addition to the above-mentioned simultaneous phase-rotation of all transversity amplitudes, which has been ruled out), which exist on continuously connected regions within the multipole parameter space [19]. These ambiguities can occur in case an insufficiently small set of observables is analyzed, and they manifest as plateau-like structures (with possibly rounded edges) in the marginalized posterior-distributions, as opposed to the peak-like structures (or modes) originating from discrete ambiguities. The set of six observables analyzed in this work (see Sec. IV) is large enough to avoid such continuous ambiguities.

For more information about discrete ambiguities in TPWA, the paper by Omelaenko [21] and especially the subsequent work [18] is recommended. The proof of the completeness of the set of six observables analyzed in this work (Sec. IV) in the idealized case of an ‘‘exact’’ TPWA⁵ proceeds a little bit different compared with the work by Omelaenko [21]. The proof is outlined in some detail in Sec. A.

Summarizing, accidental discrete ambiguities will likely be present within TPWA performed on real data, resulting in a multimodal likelihood and posterior distribution.

IV. DISCUSSION OF THE DATABASE USED

A review of the currently available database on polarization observables for the reaction $\gamma p \rightarrow \eta p$ can be found in Ref. [1]. To cover the largest possible energy range and to resolve discrete mathematical ambiguities, the TPWA is performed using the six polarization observables σ_0 [38], Σ [39], T [40], E [41], F [40], and G [42]. This choice of observables indeed resolves the discrete ambiguities of TPWA, as shown in Sec. A.

An overview of the data is given in Table III and a visualization of the phase-space coverage of the individual datasets can be found in Sec. B, Fig. 3. The available energies for the TPWA are determined by the observable with the lowest statistics [19,31], which in this case is the observable G . In total six energy bins are available, starting near the ηp -photoproduction threshold at $E_{\gamma}^{\text{lab}} = 750$ MeV up to 1250 MeV, in 100 MeV steps.

As TPWA is a single-energy regression, the energy binning of each observable has to be shifted to that of G . The procedure is described in Ref. [19]. The advantage of this method is that no new, i.e., experimentally unobserved, data points have to be constructed, for example, via interpolation.

⁵Accidental ambiguities can be disregarded for this rather academic scenario [19].

TABLE III. Information on the experimental data, given as dimensionless asymmetries, used for the TPWA of $\gamma p \rightarrow \eta p$. Energy and angular ranges are written as intervals.

Observable	Number of data points	$E_\gamma^{\text{lab}}/\text{MeV}$	$\cos(\theta)$	Facility	References
σ_0	5736	[723, 1571]	[-0.958, 0.958]	MAMI	Kashevarov <i>et al.</i> [38]
T, F	144	[725, 1350]	[-0.917, 0.917]	MAMI	Akondi <i>et al.</i> [40]
Σ	140	[761, 1472]	[-0.946, 0.815]	GRAAL	Bartalini <i>et al.</i> [39]
E	84	[750, 1350]	[-0.917, 0.917]	MAMI	Afzal <i>et al.</i> [41,43]
G	47	[750, 1250]	[-0.889, 0.667]	CBELSA/TAPS	Müller <i>et al.</i> [42]

However, none of the observables are given as profile functions which are needed for the TPWA, see Eq. (2). Thus, the angular distribution of σ_0 has to be adjusted for each observable in order to multiply both. This is not an issue, since the very precise MAMI σ_0 dataset [38] covers a large angular range [-0.958, 0.958] with a small step size ≈ 0.083 in all available energies.

The data discussed in Sec. IV not only have statistical but also systematic uncertainties. The latter ones originate primarily from the determination of the polarization degree of the photon beam and the target nucleon, the dilution factor⁶ as well as the background-subtraction procedure [38–42].

In principle, each data point has its own systematic uncertainty. However, there is no generally accepted method to model the systematic uncertainty for each data point separately. Instead, the contributions to the systematic uncertainty, which are constant over the whole angular range, are determined for each dataset. Then, the same systematic uncertainty is used for each data point within a dataset.

The contributions split up into the “general systematic uncertainty” (σ_0 : 4% [[38], p. 5]), the degree of photon beam polarization (F: 2% [40], E: 2.7% [41], G: 5% [42]), and the degree of target polarization (T, F: 4% [40], E: 2.8% [41], G: 2% [42]). The authors of the polarization observable Σ added the statistical- and systematic uncertainty in quadrature for each data point [39]. Thus, their systematic uncertainty cannot be modeled separately within this paper.

The individual systematic contributions within a dataset are combined in a conservative way. A worst-case scenario approach is employed, based on the formulas used to calculate the polarization observables, as given in the papers. In comparison with the “standard” procedure of adding the different contributions in quadrature, there are two main advantages: (1) The functional dependence is taken into account without the need to make an assumption about the distribution of the individual contributions. (2) The worst-case scenario covers the maximal and minimal impact of the systematic uncertainties, and everything in between.

As an illustrative example, suppose an observable A which depends reciprocally on the degree of polarization of the photon beam p_γ and target p_t , each with their own relative systematic uncertainty $\Delta_{\text{sys}}^{p_\gamma}$ and $\Delta_{\text{sys}}^{p_t}$, respectively. Then the

combined, relative systematic uncertainty of A would be

$$\Delta_{\text{sys}}^A = \max\left(\left|1 - (1 + \Delta_{\text{sys}}^{p_\gamma})^{-1}(1 + \Delta_{\text{sys}}^{p_t})^{-1}\right|, \left|1 - (1 - \Delta_{\text{sys}}^{p_\gamma})^{-1}(1 - \Delta_{\text{sys}}^{p_t})^{-1}\right|\right). \quad (11)$$

With the input taken from the references, corresponding to the respective datasets [38–42], the outlined approach results in $\Delta_{\text{sys}}^{\sigma_0} = 4.0\%$, $\Delta_{\text{sys}}^G = 7.4\%$, $\Delta_{\text{sys}}^E = 5.7\%$, $\Delta_{\text{sys}}^T = 4.2\%$, $\Delta_{\text{sys}}^F = 6.3\%$.

Due to the calculation of the profile functions, the systematic uncertainty of both datasets have to be combined as well:

$$\Delta_{\text{sys}}^{\check{A}} = \max\left(\left|1 - (1 + \Delta_{\text{sys}}^A)(1 + \Delta_{\text{sys}}^{\sigma_0})\right|, \left|1 - (1 - \Delta_{\text{sys}}^A)(1 - \Delta_{\text{sys}}^{\sigma_0})\right|\right). \quad (12)$$

Thus, the relative systematic uncertainties for the profile functions are $\Delta_{\text{sys}}^{\sigma_0} = 4.0\%$, $\Delta_{\text{sys}}^G = 11.7\%$, $\Delta_{\text{sys}}^E = 10.0\%$, $\Delta_{\text{sys}}^T = 8.3\%$, $\Delta_{\text{sys}}^F = 10.5\%$. The incorporation of the systematic uncertainties into the statistical model is described in more detail in Sec. V.

Furthermore, the calculation of the profile functions introduces a correlation between the unpolarized differential cross section and the profile functions, as well as among the profile functions themselves. Since certain values of $\sigma_0(W, \theta)$ were used to calculate $\check{\Sigma}^\alpha(W, \theta)$, correlations were introduced between certain data points of both observables. Moreover, the same value of $\sigma_0(W, \theta)$ might be used to calculate data points of different profile functions.

The relevance of these correlations can be estimated via the Pearson correlation coefficient [44], see Eqs. (C4) and (C5) in Sec. C. The measured values of the polarization observables are used as expectation values and the corresponding squared statistical uncertainties as the variances. An example, for a correlation matrix is shown in Fig. 4. The correlations are quite small, with absolute values below ≈ 0.17 , but typically on the order of 10^{-2} to 10^{-3} . An exception is the significantly higher correlation between σ_0 and $\sigma_0 \cdot E$, with minimal and maximal values of ≈ 0.29 and ≈ 0.67 , respectively. This can be explained by the similar definition of the coefficients $\mathcal{A}_k^\alpha(W)$ of σ_0 and $\sigma_0 \cdot E$. Both having sensitivity to almost the exact same interference terms of multipoles, albeit with different strengths (see Ref. [20]). The magnitude of the correlation matrix elements as a function of the energy can be seen in Fig. 5. The corresponding covariance matrix, which is used to construct the likelihood distribution in Sec. V A, can be estimated via Eqs. (C2) and (C3) in Sec. C.

⁶The dilution factor is the ratio of polarizable free protons to all nuclei in the used target material.

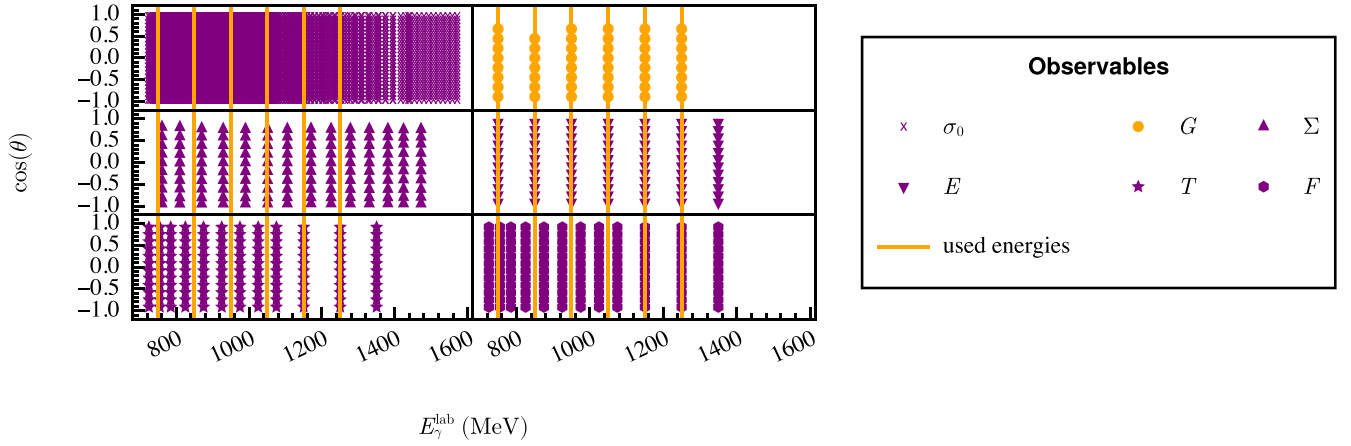


FIG. 3. Energy and angular coverage of the six observables σ_0 , Σ , G , E , T , and F [38–42] which were used for the analysis. The energies used, $E_\gamma^{\text{lab}} = [750, 850, 950, 1050, 1150, 1250]$ MeV, are determined by the observable G .

V. THE POSTERIOR DISTRIBUTION

It is assumed that the utilized profile functions, constructed from the polarization observables, follow a normal distribution. The validity of this assumption is extensively discussed in Sec. D. However, the profile functions are correlated with the unpolarized differential cross section, as well as among themselves, see Sec. IV. This dependence is modeled within the likelihood distribution using a covariance matrix. In favor of a compact representation, the functional dependencies are not shown explicitly in the subsequent equations.

A. Likelihood distribution

Combining the results of Secs. IV and D, the conditional likelihood distribution for each of the analyzed energies can

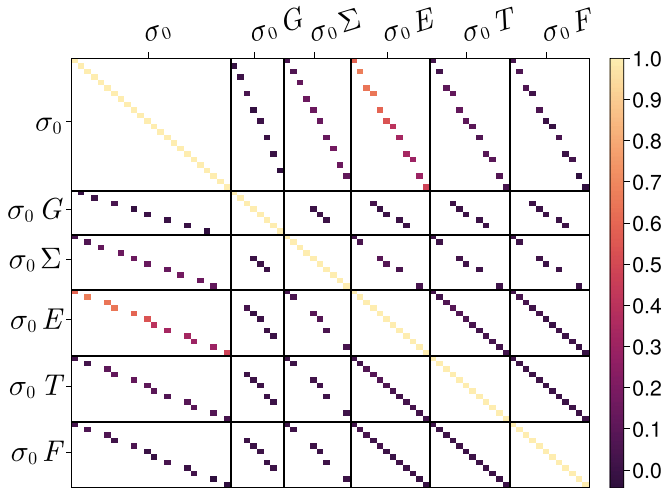


FIG. 4. Example for a correlation matrix. The correlations between the data points of the unpolarized differential cross section σ_0 and the profile functions used, as well as the correlation between the profile functions themselves, is shown for $E_\gamma^{\text{lab}} = 750$ MeV. Each square represents a certain data point. The color encodes the correlation strength ranging from -1 (darker colors) to $+1$ (lighter colors).

be formulated as an N -dimensional multivariate Gaussian distribution:

$$p(\mathbf{y}, \mathbf{x} \mid \Theta, \kappa) = \mathcal{N}(\boldsymbol{\mu}, \Lambda) = \frac{\exp\left(-\frac{1}{2}(\mathbf{y} - \boldsymbol{\mu})^T \Lambda^{-1} (\mathbf{y} - \boldsymbol{\mu})\right)}{\sqrt{(2\pi)^N |\Lambda|}}. \quad (13)$$

Herein, the vectors $\mathbf{y}, \mathbf{x} \in \mathbb{R}^N$ contain the entirety of the $N \in \mathbb{N}$ utilized profile function data points and the corresponding $\cos(\theta)$ values at which they were measured, respectively:

$$\mathbf{y} = [y^{\sigma_0}, y^{\check{G}}, y^{\check{\Sigma}}, y^{\check{E}}, y^{\check{T}}, y^{\check{F}}], \quad (14)$$

$$\mathbf{x} = [x^{\sigma_0}, x^{\check{G}}, x^{\check{\Sigma}}, x^{\check{E}}, x^{\check{T}}, x^{\check{F}}]. \quad (15)$$

The parameters of the model can be divided into two groups. On the one hand, the real- and imaginary parts of multipoles, i.e., Eq. (4), denoted by $\Theta \in \mathbb{R}^{8\ell_{\text{max}}-1}$ are used to

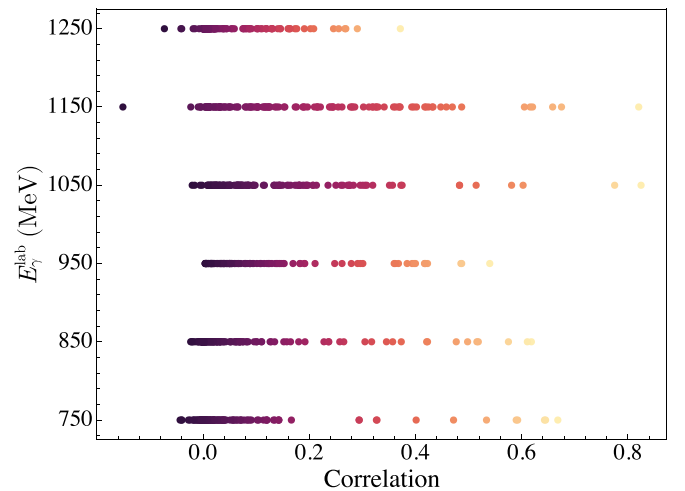


FIG. 5. Unique correlation matrix element values as a function of the laboratory frame energy. The color encodes the correlation strength ranging from -1 (darker colors) to $+1$ (lighter colors).

model the underlying physical process. On the other hand, the parameters $\kappa \in \mathbb{R}^5$ which are used to model the systematic uncertainties of the involved datasets:

$$\kappa = [\kappa^{\sigma_0}, \kappa^{\check{G}}, \kappa^{\check{E}}, \kappa^{\check{T}}, \kappa^{\check{F}}]. \quad (16)$$

The multivariate normal distribution in Eq. (13) is constructed with the model predictions $\mu \in \mathbb{R}^N$ for the expectations of y :

$$\begin{aligned} \mu(\Theta, \kappa, \mathbf{x}) \\ = [\kappa^{\sigma_0} \mu^{\sigma_0}, \kappa^{\check{G}} \mu^{\check{G}}, 1 \mu^{\check{\Sigma}}, \kappa^{\check{E}} \mu^{\check{E}}, \kappa^{\check{T}} \mu^{\check{T}}, \kappa^{\check{F}} \mu^{\check{F}}]. \end{aligned} \quad (17)$$

The $\mu^\alpha(\Theta, \mathbf{x}^\alpha)$ are the model predictions for the individual profile functions, i.e., Eq. (2). Hence, in order to model the systematic uncertainties, one additional parameter per relevant dataset is introduced and multiplied with the corresponding theoretical prediction for the profile function. Thus, the model gets additional degrees of freedom to adjust for possible systematic uncertainties. However, these parameters are restricted to physical meaningful bounds, further discussed in Sec. VB. As explained in Sec. IV, the systematic uncertainty of the polarization observable Σ cannot be modeled.

Finally, there is the covariance matrix $\Lambda \in \mathbb{R}^{N \times N}$. Its off-diagonal terms are not identical, and therefore the data pairs are not exchangeable.⁷

B. Prior distribution

The priors for the multipole parameters are chosen as uniform priors with bounds corresponding to the physically allowed ranges of the parameters (see Ref. [19]). Thus, the priors incorporate physical knowledge while being uninformative compared with the likelihood distribution.

In principle a uniform prior for the systematic parameters would be reasonable. However, in this case the hard boundaries in the parameter space lead to numerical issues. Thus, the prior distributions for the scaling parameters κ are assumed to be normally distributed and centered around the value one. The standard deviation is chosen such that⁸ 99% of the distribution are within the range $1 \pm \Delta_{\text{sys}}^\alpha$, which results in (rounded to five digits):

$$\kappa^{\sigma_0} \sim \mathcal{N}(1, 0.01552), \quad (18)$$

$$\kappa^{\check{G}} \sim \mathcal{N}(1, 0.04542), \quad (19)$$

$$\kappa^{\check{E}} \sim \mathcal{N}(1, 0.03882), \quad (20)$$

$$\kappa^{\check{T}} \sim \mathcal{N}(1, 0.03222), \quad (21)$$

$$\kappa^{\check{F}} \sim \mathcal{N}(1, 0.04076). \quad (22)$$

⁷If the joint probability density function $p(y, \mathbf{x} | \Theta, \kappa)$ is invariant under permutations of the data pairs $(y, x)_i$, then the data pairs are said to be exchangeable [23,45].

⁸This can be calculated by solving numerically the following equation for the standard deviation σ :

$$\int_{-\infty}^{1-\Delta_{\text{sys}}^\alpha} \frac{\exp\left(-\frac{1}{2}\left(\frac{x-1}{\sigma}\right)^2\right)}{\sigma\sqrt{2\pi}} dx = \frac{1-0.99}{2}.$$

This choice is in accordance with the conservative combination of the systematic uncertainties, as discussed in Sec. IV. The treatment of systematic errors within this paper is similar to that in Refs. [31,46,47].

VI. RESULTS

Bayesian inference was utilized to extract the electromagnetic multipole parameters, as introduced in Eq. (4), for the reaction $\gamma p \rightarrow \eta p$ at energies $E_\gamma^{\text{lab}} = [750, 850, 950, 1050, 1150, 1250]$ MeV and truncation orders $\ell_{\text{max}} = 1, 2$ through truncated partial-wave analysis. The procedures involved are detailed in Sec. E.

Highly multimodal posterior distributions were encountered, necessitating an adaptation of the typical MCMC convergence diagnostic workflow. The adjusted procedure is detailed in Sec. E3. By studying the reproduced data distributions for the various truncation orders, an indication of N^* resonances in the energy range from 950 to 1050 MeV is observed. Finally, utilizing the electromagnetic multipole parameter estimates, predictions were calculated⁹ for the polarization observables H and P as well as those of group \mathcal{BR} and \mathcal{TR} . Hence, this includes eight polarization observables that are yet to be measured. The distributions of the multipole parameters, the reproduced and predicted data are presented alongside the values of EtaMAID2018 [48], BnGa-2019 [42], and JüBo-2022 [47].

The presentation of the multipole parameter results is quite detailed and deserves an explanation. The top part shows the solutions found via Monte Carlo maximum *a posteriori* estimation and their corresponding χ^2/ndf values, together with the 1σ uncertainty (see Sec. E1). The middle part shows the marginal-parameter distributions obtained via Bayesian inference, as explained in Secs. V and E2. For a better comparison of the two approaches for $\ell_{\text{max}} = 1$, the [0.16, 0.5, 0.84] quantiles of the distributions, corresponding to the median of the distribution and the 1σ -uncertainty boundaries, are drawn as dashed lines through all parts of the figure. Whereas, for $\ell_{\text{max}} = 2$ a solid vertical line is drawn for each peak of the multimodal distribution, i.e., the most probable values. The bottom part of the figure is a contour plot of the log posterior density distribution and the corresponding marginal-parameter distribution. The outermost contour line is at 1% of the maximum altitude, each subsequent line represents an 11% increase. It is assumed that a log posterior distribution centered around a higher log posterior value, corresponds to more likely parameter values because this solution contributes more probability mass to the posterior. Each solution group is drawn in a different color and each peak of a distribution corresponds to an accidental ambiguity. The color for a specific solution group is consistent between the shown figures (MCMC convergence, multipole, predictive performance plots, etc.) for a certain energy and truncation order. This

⁹To get from the profile functions to the dimensionless polarization observables, the predicted distribution is divided by a certain σ_0 value, corresponding to the $\cos(\theta)$ value at which the prediction were calculated.

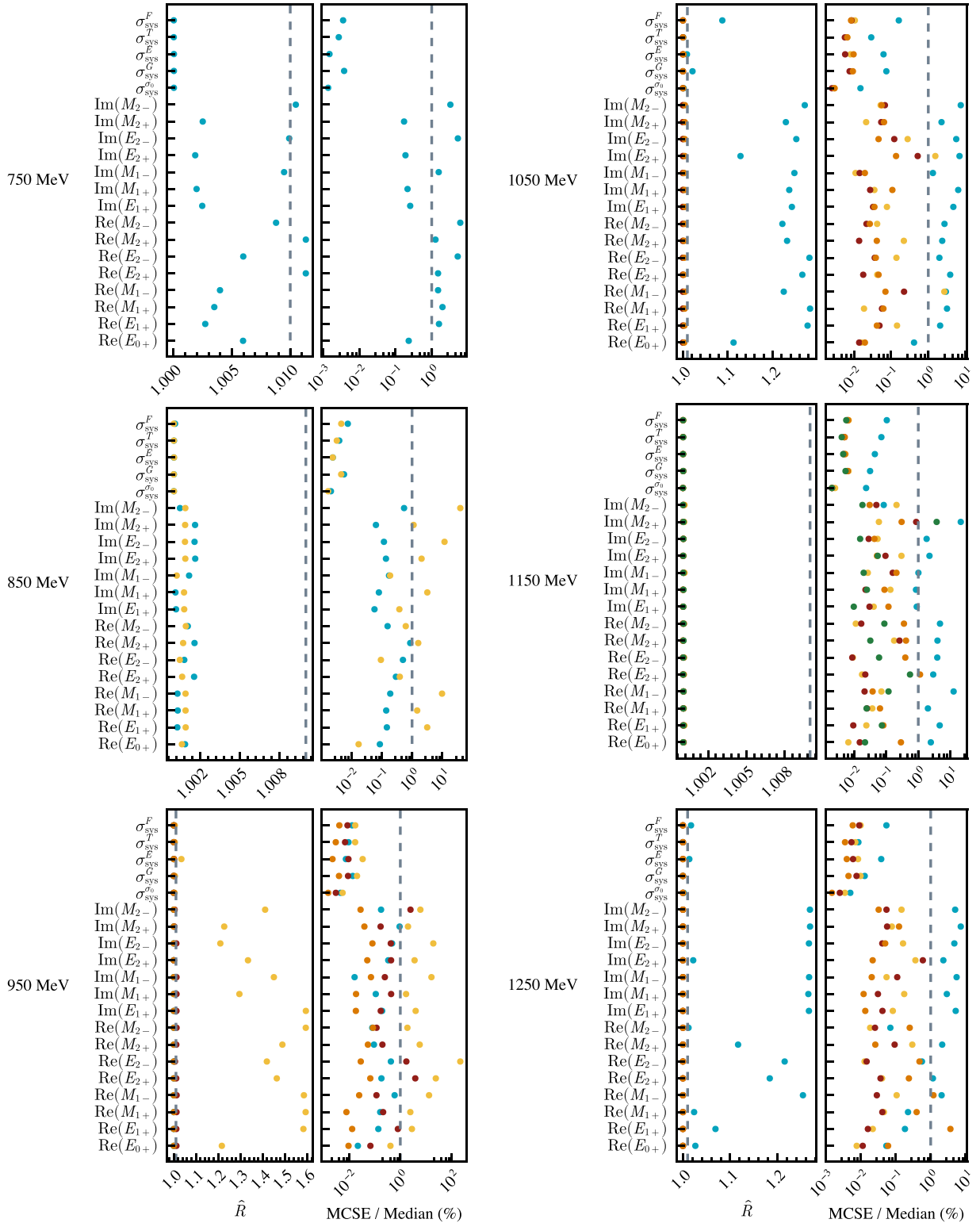


FIG. 6. MCMC convergence diagnostics for the truncation order $\ell_{\max} = 2$. Shown are the potential-scale-reduction statistic \hat{R} (the gray, dashed line indicates the value of 1.01) and the Monte Carlo standard error (MCSE) for the median divided by the median in percent (the gray, dashed line indicates the value of 1%). Each solution group is drawn in a different color.

means one can monitor the behavior of a specific ambiguity, ranging from the MCMC diagnostic plots in Fig. 6 to the multipole plots in Figs. 7 and 8, to the reproduced data plots in Fig. 2, up to the predicted data distribution plots in Fig. 9. The

performed analyses showed, that Bayesian inference gives more insight into the relevance of ambiguities, due to the Hamiltonian Monte Carlo algorithm. When multiple chains sample consistently multiple marginal modes together, this

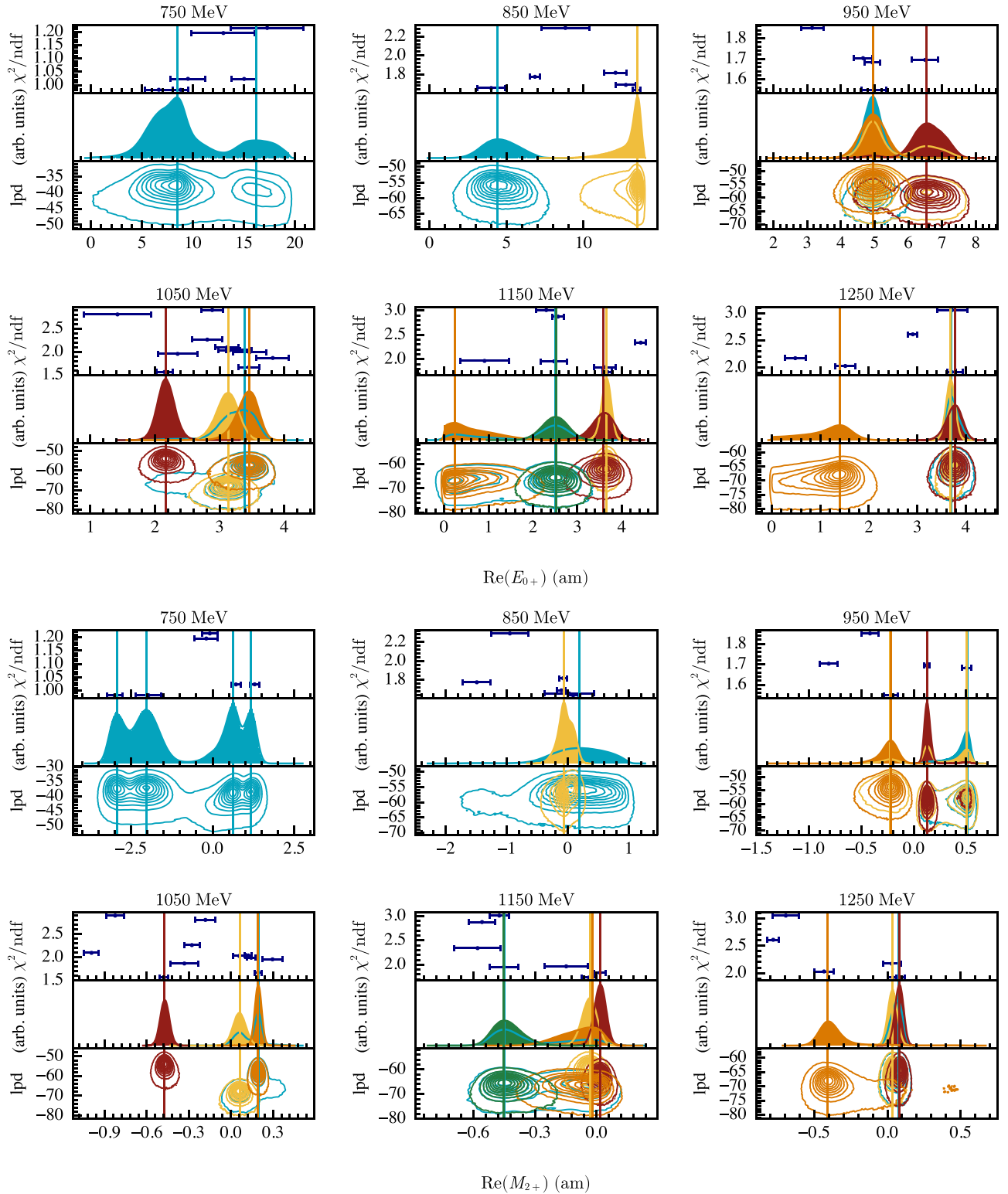


FIG. 7. Solutions of the multipole parameters $\text{Re}(E_{0+})$ and $\text{Re}(M_{2+})$ for a truncation order of $\ell_{\text{max}} = 2$, for the energy bins $E_{\gamma}^{\text{lab}} = [750, 850, 950, 1050, 1150, 1250]$ MeV. Each solution group is drawn in a different color and each peak of a distribution corresponds to an accidental ambiguity. The different parts of the tripartite plots are explained at the beginning of Sec. VI. The natural logarithm was used to calculate the log posterior density (lpd).

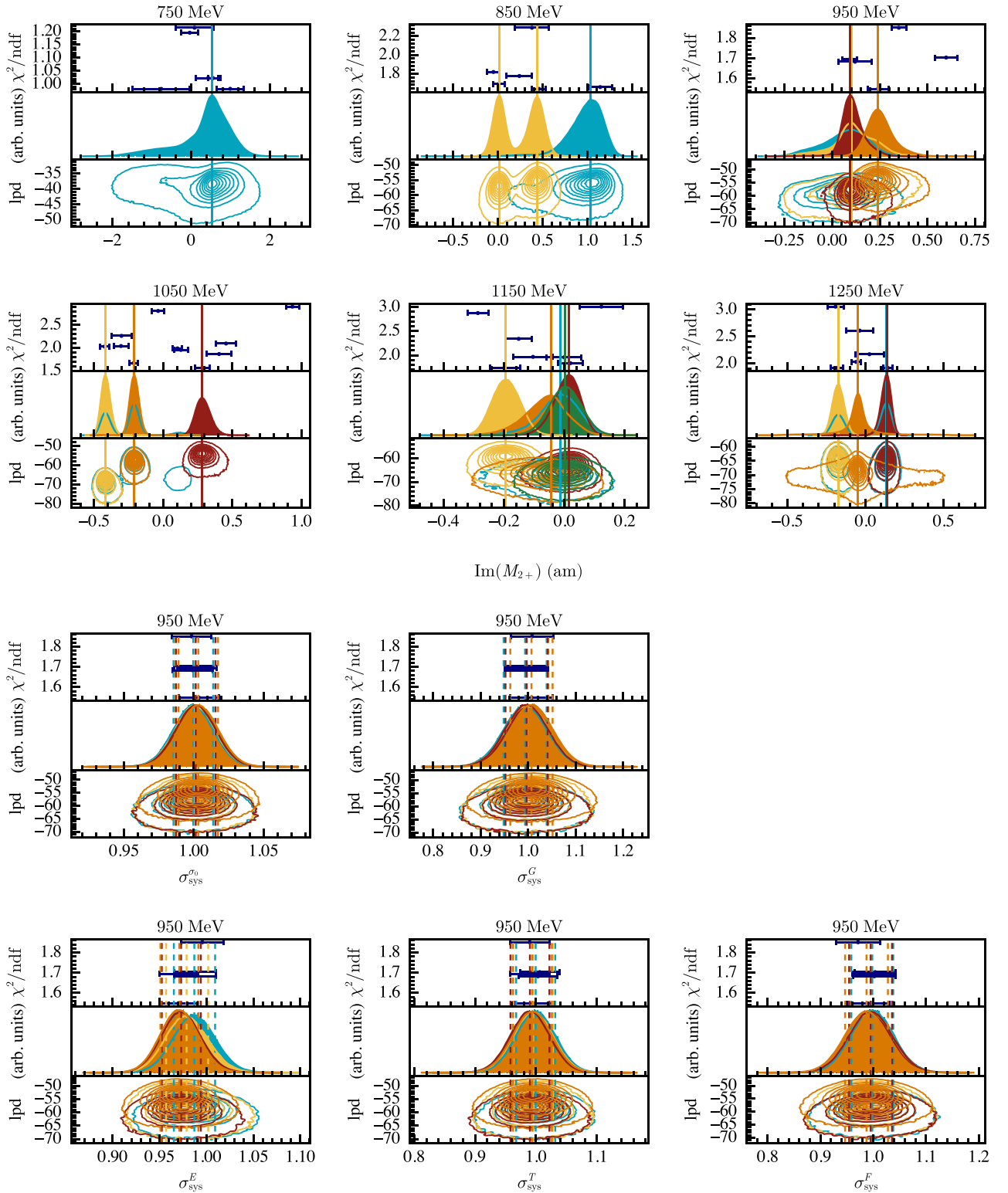


FIG. 8. Solutions of the multipole parameter $\text{Im}(M_{2+})$ for a truncation order of $\ell_{\text{max}} = 2$, for the energy bins $E_{\gamma}^{\text{lab}} = [750, 850, 950, 1050, 1150, 1250]$ MeV. In addition, solutions of systematic parameters for a truncation order of $\ell_{\text{max}} = 2$ for the energy bin $E_{\gamma}^{\text{lab}} = 950$ MeV are shown. Each solution group is drawn in a different color and each peak of a distribution corresponds to an accidental ambiguity. The different parts of the tripartite plots are explained at the beginning of Sec. VI. The natural logarithm was used to calculate the log posterior density (lpd).

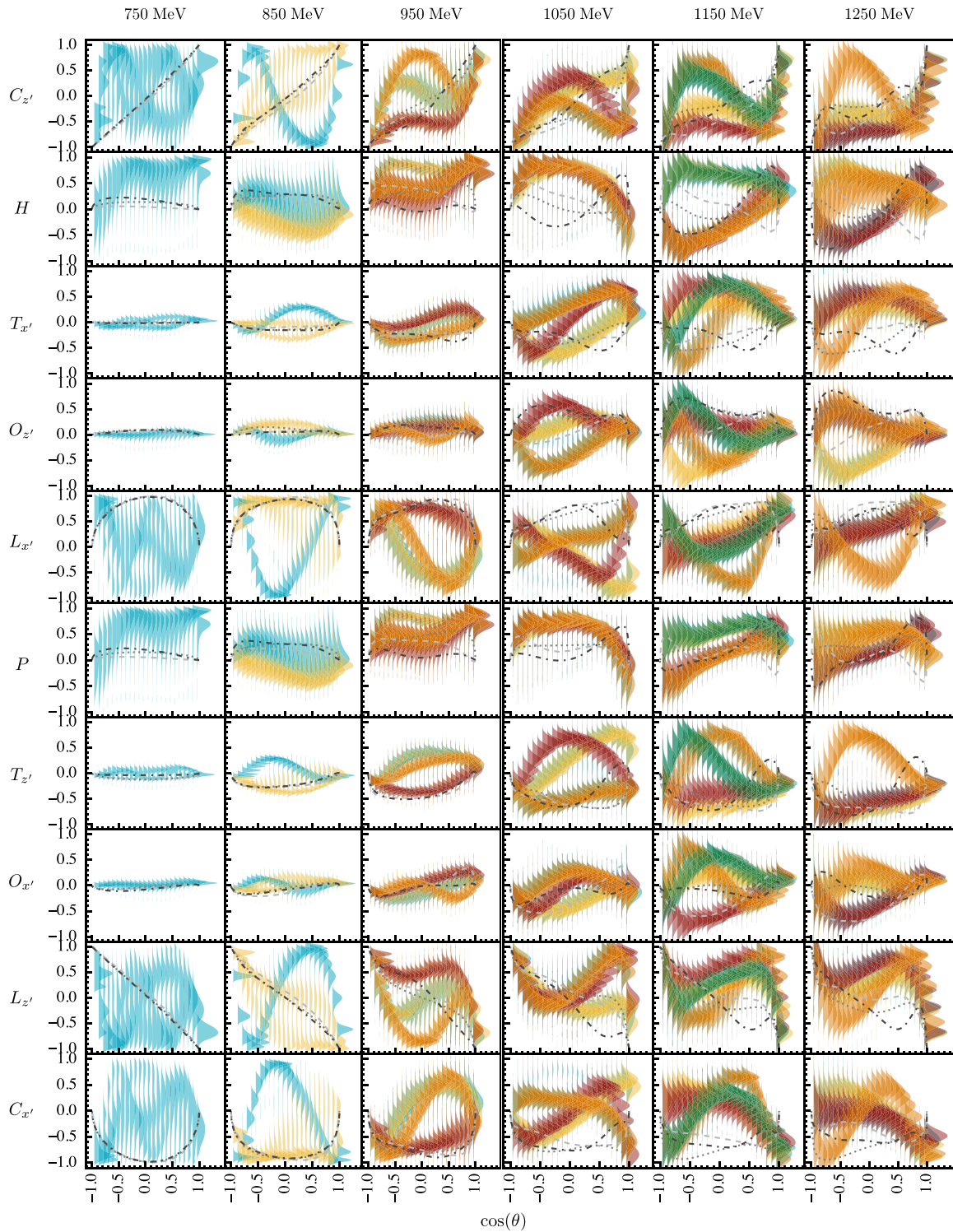


FIG. 9. Predicted data distributions for the polarization observables C_z' , H , T_x' , O_z' , L_x' , P , T_z' , O_x' , L_z' , and C_x' for the energy bins $E_\gamma^{\text{lab}} = [750, 850, 950, 1050, 1150, 1250]$ MeV, using a truncation order of $\ell_{\text{max}} = 2$. Each solution group is drawn in a different color and each peak of a distribution corresponds to an accidental ambiguity. In addition, the corresponding values from EtaMAID2018 [48] (dashed line), BnGa-2019 [42] (dotted line), and JüBo-2022 [47] (dash-dotted line) are shown as well.

is a sign of a problematic ambiguity, as they tend to have comparable log posterior densities. As an example, consider the multipole solution for $\text{Re}(M_{2+})$ at 750 MeV in Fig. 7. This is an advantage over the maximum likelihood approach.

Within the following discussion of the results a representative selection of figures is shown. All parameter figures, for all analyzed energies and truncation orders can be found in the Supplemental Material [49].

A. Impact of accidental ambiguities on the results

As discussed in Sec. III A, accidental ambiguities appear in the results of the marginal multipole parameter distributions, which subsequently manifest in both the replicated and predicted data distributions, as well as in the marginal systematic parameter distributions. The ambiguities are apparent as differently colored distributions, where each peak of a distribution corresponds to an accidental ambiguity. See, for example, 2 and 7 to 9. As expected, all accidental ambiguities can replicate the original data points. The corresponding reproduced data distributions are nearly identical, as illustrated in Fig. 2. The impact of ambiguities on predicted data distributions and what can be learned from it is discussed in Sec. VI F.

B. Choice of the truncation order

At first, the regression was conducted using $\ell_{\max} = 1$. For each of the six energy bins, the number of warmup and post-warmup samples was set to 2×10^4 , respectively. In total, $N_c = 10$ chains are started at each solution, found via the Monte Carlo maximum *a posteriori* approach. The corresponding MCMC convergence diagnostics, displayed in Sec. F, Fig. 10, support this decision, with $\hat{R} < 1.01$ and relative Monte Carlo standard error within a few percent or less.

For each energy bin above 950 MeV, specifically 1050, 1150, and 1250 MeV, the measured σ_0 data are systematically higher for $\cos(\theta) > 0$ compared with the TPWA predictions. Furthermore, the TPWA predictions for $\check{\Sigma}$ do not resemble the original data points at all, as shown in Fig. 1. It appears that the statistical model utilized with truncation order $\ell_{\max} = 1$ cannot adequately replicate data points for all observables. An elucidation for this phenomenon is provided in Sec. VI C.

To enhance the data description flexibility of the TPWA model, the truncation order was increased to $\ell_{\max} = 2$, and the regression was re-executed. To obtain the desired MCMC convergence diagnostics for each of the six energy bins, it was necessary to increase the number of warmup and postwarmup samples to 5×10^4 , respectively. N_c remains the same as for $\ell_{\max} = 1$. The corresponding MCMC convergence diagnostics are displayed in Sec. F, Fig. 6. Special phenomena that occur are discussed in detail in Sec. F. The TPWA model with a truncation order of $\ell_{\max} = 2$ effectively describes the original data points as evinced by the data distributions reproduced in Fig. 2.

In general, it is preferable to set the truncation order ℓ_{\max} as high as possible, because lower partial waves can interfere with higher ones, leading to non-negligible contributions. However, increasing the truncation order also increases the number of accidental ambiguities. For example, with $\ell_{\max} = 3$ and 1250 MeV, 43 posterior modes were identified. This results in a situation that demands a large number of numerical computations to achieve the desired MCMC convergence diagnostics. Additionally, the visual assessment of clustering becomes challenging due to the large number of required chains. Furthermore, the statistical quality of the combined datasets do not permit observations of any *F*-wave contributions, such as those from the $N(1680)5/2^+$ [2] resonance at $E_\gamma^{\text{lab}} \approx 1035$ MeV. Due to these considerations, this paper

focuses on $\ell_{\max} = 2$, while truncation orders with $\ell_{\max} > 2$ are reserved for future research.

C. Indication of N^* resonances

To summarize, the model with $\ell_{\max} = 1$ is inadequate in replicating the original data points for σ_0 and $\check{\Sigma}$ for the energies above 950 MeV. This phenomenon could be explained by an emerging resonance in the energy range between 950 and 1050 MeV that couples to an orbital angular momentum $\ell > 1$ and predominantly contributes to σ_0 and $\check{\Sigma}$. Since isospin is a conserved quantity in the strong interaction, the reaction of η photoproduction serves as an isospin filter, meaning that for the subsequent discussion, only N^* resonances require consideration. There are two N^* resonances which fulfill the conservation laws, couple to $\ell = 2$, and fall within the required energy range (taking into account the Breit-Wigner width [2] of the resonances). These resonances are $N(1675)5/2^-$ [2] at $E_\gamma^{\text{lab}} \approx 1026$ MeV and $N(1700)3/2^-$ [2] at $E_\gamma^{\text{lab}} \approx 1071$ MeV.

There is also a resonance which opens up already at $E_\gamma^{\text{lab}} \approx 762$ MeV, specifically $N(1520)3/2^-$ [2]. However, this resonance has a branching ratio to ηN [2] that is ≈ 10 times smaller than those of $N(1675)5/2^-$ and $N(1700)3/2^-$. The datasets employed do not appear to possess the necessary sensitivity to see a contribution of $N(1520)3/2^-$.

D. Multipole parameters

The solutions for E_{0+} and M_{2+} are shown as representative examples of the multipole parameters in Figs. 7 and 8. The figures for all multipole parameters are available in the Supplemental Material [49]. Typically, the peaks of the marginal distributions are in agreement with the first few “best” *a posteriori* estimates. However, not every *a posteriori* solution has a corresponding peak within the marginal distributions. This could be due to two potential reasons. On the one hand, the interpretation of a marginal distribution differs from that of a maximum *a posteriori* estimate. On the other hand, the reason may lie within the Hamiltonian Monte Carlo algorithm [26,27], where it has been observed that some of the starting values are not in close proximity to the “typical set”¹⁰ [50] but adjust rapidly. An example is shown in Fig. 11.

Within Fig. 12, the fifteen multipole parameters are graphed based on the laboratory energy of the photon. The corresponding values of EtaMAID2018 [48], BnGa-2019 [42], and JüBo-2022 [47] are also shown. For a detailed comparison of the various solution clusters and their relevance, readers are encouraged to refer to the tripartite multipole parameter figures in Figs. 7 and 8 and the Supplemental Material in Ref. [49].

¹⁰The “typical set” are the regions of the posterior which contribute the most to its expectation value.

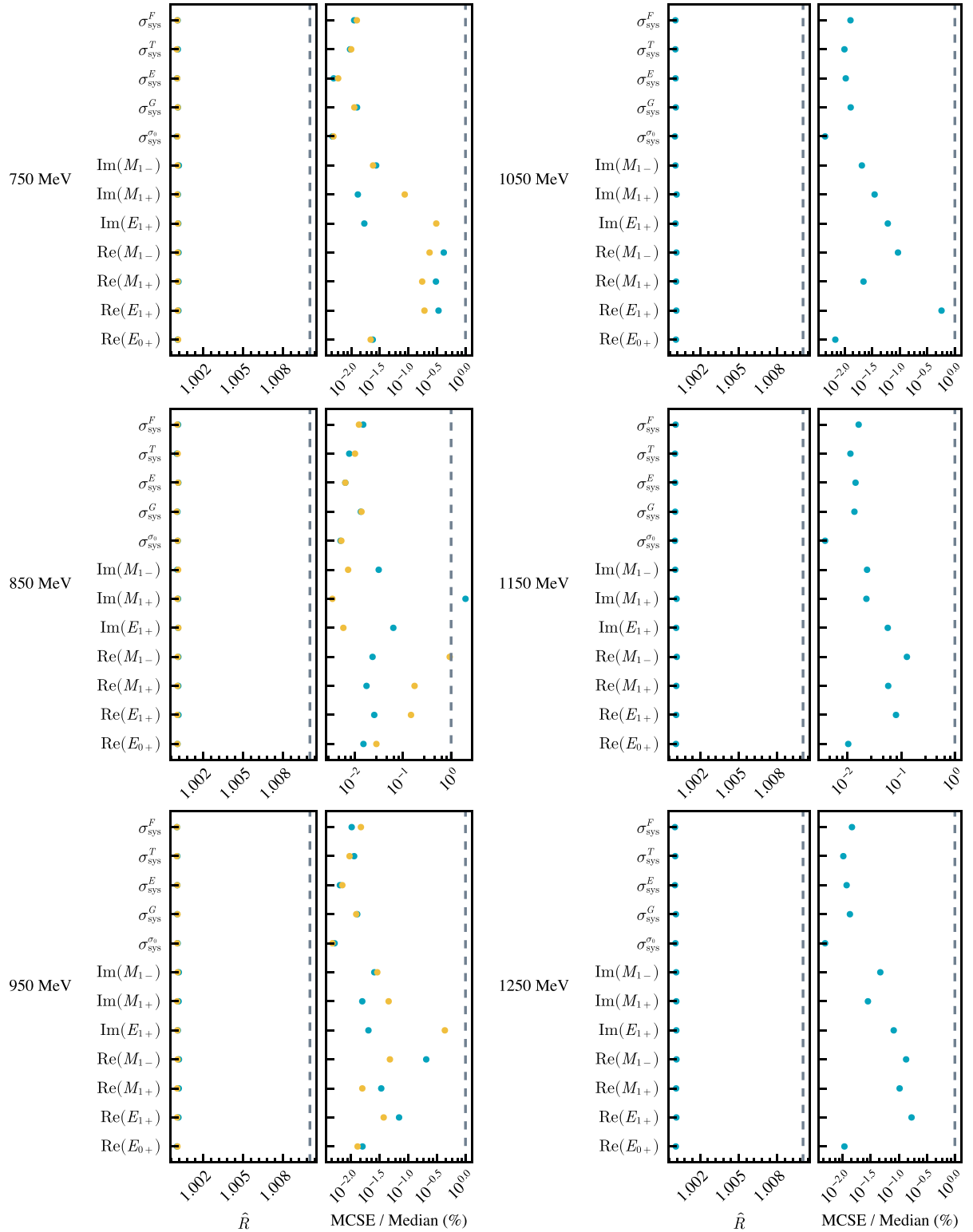


FIG. 10. MCMC convergence diagnostics for the truncation order $\ell_{\max} = 1$. Shown are the potential-scale-reduction statistic \hat{R} (the gray, dashed line indicates the value of 1.01) and the Monte Carlo standard error (MCSE) for the median divided by the median in percent (the gray, dashed line indicates the value of 1%). Each solution group is drawn in a different color.

d1. Comparison with MAID, BnGa, and JuBo

In general, the paper's results align well with the values of EtaMAID2018, BnGa-2019, and JüBo-2022. However, there are two noteworthy exceptions.

First, for the multipole parameter $\text{Im}(E_{2+})$, none of the PWA values align with each other nor with the TPWA results of this paper. Second, the three PWAs report a value of ≈ 20 mfm for the multipole parameter $\text{Re}(E_{0+})$ at 750 MeV. This

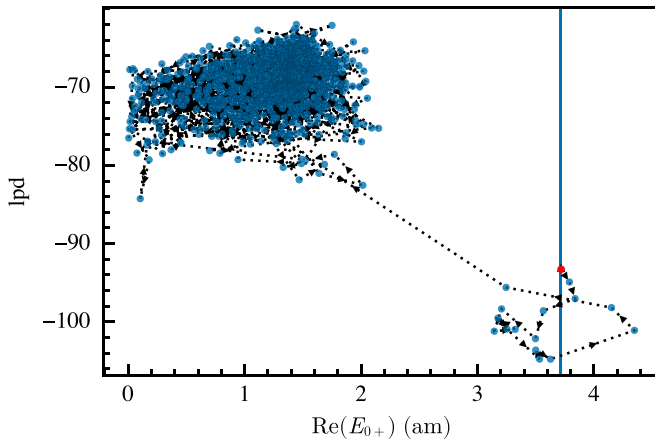


FIG. 11. Illustration of the first 1000 sampling points of a chain with initial value at 3.7 (the blue vertical line). The first sampling point is drawn in red. The chain converges from its starting point to a more likely solution, i.e., with higher log posterior density (lpd) value. The natural logarithm was used to calculate the lpd.

significant value of E_{0+} close to the ηp -production threshold results from the dominant $N(1535)1/2^-$ resonance, which couples to the S -wave E_{0+} . The datasets of η photoproduction (see Sec. IV) utilized in this analysis do not emphasize such high values. Although the marginal parameter distribution does indeed have a nonzero probability at ≈ 19 mfm, the most likely values are around 8.5 mfm. This unexpected difference may have multiple causes. On the one hand, both BnGa-2019 and JüBo-2022 are coupled-channel analyses that involve a variety of final states simultaneously [14]. On the other hand, EtaMAID2018, BnGa-2019, and JüBo-2022 use the πN partial-wave amplitudes from SAID [14] as input, which includes the $N(1535)1/2^-$ resonance [51].

In contrast, the current analysis is not a coupled-channel analysis nor does it rely on the SAID solutions. The values of the multipole parameters are exclusively obtained from the η -photoproduction datasets presented in Sec. IV.

In addition, the TPWA relies on single-energy regression, which implies that solely the available data points at a particular energy bin can be utilized in the analysis. As the PWAs do not follow this restriction, the complete available datasets can be utilized. This is particularly important for the differential cross section, where the increased data can have a significant impact on the regression.

Furthermore, although a dominant S -wave E_{0+} results in a nearly constant maximal allowed value of one for the observable E for all angles, the inverse conclusion does not always hold true. For example, the observable E cannot differentiate between S -wave E_{0+} and P -wave M_{1-} since both can lead to these maximum values of E . As shown in our results for 750 MeV (see Fig. 12), the expected strength of E_{0+} has migrated to other multipoles, such as M_{1-} .

Improved statistics of the datasets involved in terms of the angular range or the inclusion of additional observables in future analyses, may shift the probability mass of the distribution of $\text{Re}(E_{0+})$ at 750 MeV towards the values of EtaMAID2018, BnGa-2019, and JüBo-2022.

E. Systematic parameters

The systematic parameters are all around the intended value of one. Each marginal distribution, for all systematic parameters and for all analyzed energy bins, is exclusively unimodal. Examples can be found in Fig. 8 and the Supplemental Material [49].

F. Predicted data distributions

Using the estimated multipole parameters, predictions for polarization observables were calculated which were not utilized in this analysis. These include the observables H , P as well as all eight observables of the groups \mathcal{BR} and \mathcal{TR} that have yet to be measured [1]. The predicted data distributions are displayed in Fig. 9. The distributions are within the physical bounds between -1 and 1 and their overall course over the angular range shows the correct tendency at $\cos(\theta) = \pm 1$ towards the mathematically expected values [18].

An interesting effect can be observed. The predicted data distributions for the various ambiguities, show specific functional trajectories over the angular range. In contrast, for the reproduced data plots, the distributions were almost identical for different ambiguities. If there were experimental data related to one of the predicted observables that supports only one of the specific functional trends throughout the angular range, it would eliminate any other ambiguity.

According to this criterion, potentially significant polarization observables have been chosen for upcoming experiments and are consolidated in Table IV. In particular, the polarization observable C_z' seems suitable to reduce the ambiguities at all six energy bins.

VII. SUMMARY AND OUTLOOK

A TPWA was conducted for η -meson photoproduction off the proton near the production threshold. Model-independent estimates of electromagnetic multipole parameters were determined, allowing the first model-independent calculation of predictions of unmeasured polarization observables. Based on these results, promising future measurements were identified with the aim of minimizing remaining ambiguities.

The datasets used in this study demonstrate clear D -wave contributions above $E_\gamma^{\text{lab}} = 950$ MeV, but are not sensitive to F -wave or higher partial-wave contributions.

For the first time, this study combined TPWA with Bayesian inference. The posterior distributions were highly multimodal, necessitating adaptations to monitor the MCMC convergence diagnostics. Despite its simplicity and use of fewer data, the TPWA approach maintains model-independence and achieves results consistent with the PWAs of MAID2018, BnGa-2019, and JüBo-2022.

In general, resonances can be extracted from multipole parameters. However, for a precise extraction of the resonance parameters the current resolution of the combined datasets is not sufficient. In a subsequent study, the TPWA approach could be combined with the Laurent + Pietarinen parametrization for every multipole parameter [52] in order

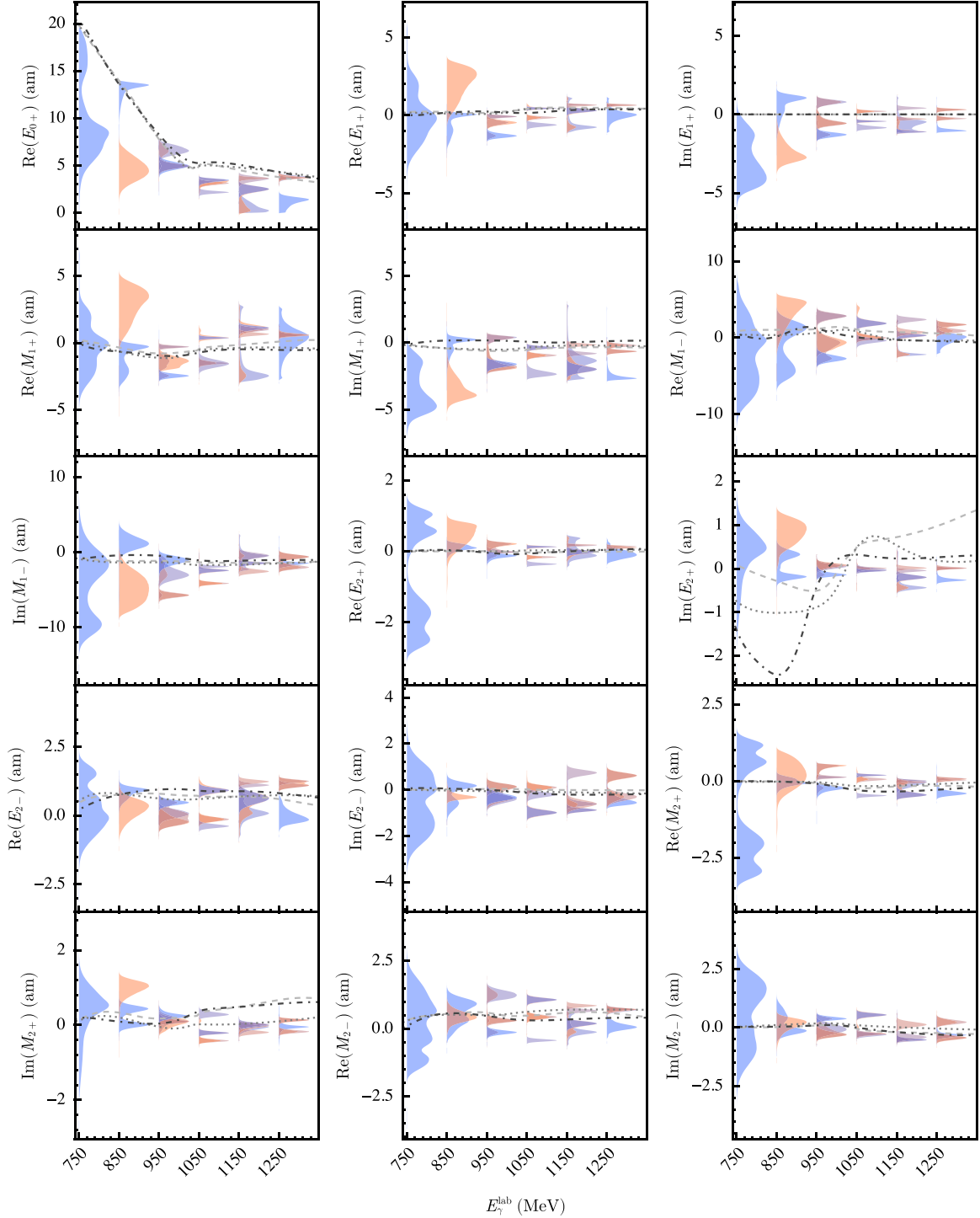


FIG. 12. Marginal multipole solutions for the truncation order $\ell_{\max} = 2$ for the energy bins $E_{\gamma}^{\text{lab}} = [750, 850, 950, 1050, 1150, 1250]$ MeV. In addition, the multipole parameter predictions from EtaMAID2018 [48] (dashed line), BnGa-2019 [42], (dotted line) and JüBo-2022 [47] (dash-dotted line) are shown as well. The relevance of a solution is represented by a transition from sienna (less relevant) to blue (more relevant) hues. However, for a detailed comparison between the solutions and their relevance to each other, the reader is advised to the tripartite multipole parameter figures in Figs. 7 and 8 and Ref. [49].

to extract resonance parameters. In addition, the role of the prior distribution with regard to resolving the mathematical ambiguities could be investigated.

ACKNOWLEDGMENTS

The authors would like to thank Professor Dr. Sebastian Neubert, Professor Dr. Carsten Urbach, and Dr. Jan Hartmann

TABLE IV. Promising polarization observable candidates to resolve the ambiguities for truncation order $\ell_{\max} = 2$. The corresponding predicted data distributions are shown in Fig. 9.

E_{γ}^{lab} (MeV)	Observables
750	$C_{z'}^{\prime}, C_{x'}^{\prime}, L_{x'}^{\prime}, L_{z'}^{\prime}$
850	$C_{z'}^{\prime}, C_{x'}^{\prime}, L_{x'}^{\prime}, L_{z'}^{\prime}, T_{x'}^{\prime}, T_{z'}^{\prime}$
950	$C_{z'}^{\prime}, C_{x'}^{\prime}, L_{x'}^{\prime}, L_{z'}^{\prime}, T_{z'}^{\prime}$
1050	$C_{z'}^{\prime}, C_{x'}^{\prime}, L_{x'}^{\prime}, O_{z'}^{\prime}, T_{z'}^{\prime}$
1150	$C_{z'}^{\prime}, O_{x'}^{\prime}, T_{x'}^{\prime}, T_{z'}^{\prime}$
1250	$C_{z'}^{\prime}$

for several fruitful discussions. Furthermore, special thanks go to Professor Dr. Reinhard Beck for his support.

APPENDIX A: DISCRETE AMBIGUITIES OF THE ANALYZED SET OF SIX POLARIZATION OBSERVABLES

Within this Appendix, the discrete partial-wave ambiguities of the six observables $\{\sigma_0, \check{\Sigma}, \check{T}, \check{F}, \check{G}, \check{E}\}$ analyzed within this work (cf. Sec. IV and Table III) are discussed. It is argued that this specific set is mathematically complete in a TPWA. As has been demonstrated already in other works (e.g., Ref. [19]), such mathematical considerations can still serve as a useful precursor to analyses of real data.

The following discussion is based on the ‘‘Omelaenko formalism’’ [21]. The basic definitions of the sixteen observables in pseudoscalar meson photoproduction, expressed in the transversity basis, are used. The expressions are collected in Table II.

1. Discrete ambiguities of the group- \mathcal{S} observables in truncated partial-wave analysis

As is well known from Omelaenko’s work, in the case of a truncated partial-wave analysis with maximum angular momentum ℓ_{\max} , the four transversity amplitudes can be expressed in terms of linear factorizations:

$$b_1(\theta) = -C a_{2L} \frac{\exp(-i\frac{\theta}{2})}{(1+t^2)^L} \prod_{k=1}^{2L} (t + \beta_k), \quad (\text{A1})$$

$$b_2(\theta) = -C a_{2L} \frac{\exp(i\frac{\theta}{2})}{(1+t^2)^L} \prod_{k=1}^{2L} (t - \beta_k), \quad (\text{A2})$$

$$b_3(\theta) = C a_{2L} \frac{\exp(-i\frac{\theta}{2})}{(1+t^2)^L} \prod_{k=1}^{2L} (t + \alpha_k), \quad (\text{A3})$$

$$b_4(\theta) = C a_{2L} \frac{\exp(i\frac{\theta}{2})}{(1+t^2)^L} \prod_{k=1}^{2L} (t - \alpha_k), \quad (\text{A4})$$

where $t = \tan(\theta/2)$ (with the center-of-mass scattering angle θ) and $\{\alpha_k, \beta_k\}$ are the Gersten-Omelaenko roots, which are, in essence, equivalent to multipoles.

Furthermore, all permissible solutions have to satisfy Omelaenko’s constraint, i.e., Eq. (10). The solution theory for the case where all four group- \mathcal{S} observables have been selected, and thus only ambiguities of the four moduli $|b_1|, |b_2|, |b_3|, |b_4|$ have to be considered, has been worked out at length in

Ref. [19]. This solution theory leads to the known complete sets of five (e.g., $\{\sigma_0, \check{\Sigma}, \check{T}, \check{P}, \check{F}\}$). In the following section, the special case where less than four diagonal observables are selected is considered.

2. Discrete ambiguities of the three group- \mathcal{S} observables $\{\sigma_0, \Sigma, T\}$

The set of observables used within this work contains only three simultaneously diagonalized observables ($\sigma_0, \check{\Sigma}, \check{T}$, see Table II). Therefore, one has to investigate which kinds of discrete ambiguities are allowed by this set of three observables, using the root-formalism described in Appendix A 1. For this purpose, one can look at the ‘‘minimal’’ linear combinations of squared moduli:

$$\sigma_0 - \check{\Sigma} = 2(|b_1|^2 + |b_2|^2), \quad (\text{A5})$$

$$\sigma_0 + \check{\Sigma} = 2(|b_3|^2 + |b_4|^2), \quad (\text{A6})$$

$$\sigma_0 + \check{T} = 2(|b_1|^2 + |b_4|^2), \quad (\text{A7})$$

$$\sigma_0 - \check{T} = 2(|b_2|^2 + |b_3|^2), \quad (\text{A8})$$

$$-\check{\Sigma} + \check{T} = 2(|b_1|^2 - |b_3|^2), \quad (\text{A9})$$

$$-\check{\Sigma} - \check{T} = 2(|b_2|^2 - |b_4|^2). \quad (\text{A10})$$

Upon reducing the problem to the nonredundant amplitudes b_2 and b_4 in the TPWA [by using $b_4(W, \theta) = b_3(W, -\theta)$ and $b_2(W, \theta) = b_1(W, -\theta)$, cf. Eq. (6) to (9)], one obtains

$$\sigma_0 - \check{\Sigma} \propto \prod_{k=1}^{2\ell_{\max}} (t + \alpha_k^*)(t + \alpha_k) + \prod_{k=1}^{2\ell_{\max}} (t - \alpha_k^*)(t - \alpha_k), \quad (\text{A11})$$

$$\sigma_0 + \check{\Sigma} \propto \prod_{k=1}^{2\ell_{\max}} (t + \beta_k^*)(t + \beta_k) + \prod_{k=1}^{2\ell_{\max}} (t - \beta_k^*)(t - \beta_k), \quad (\text{A12})$$

$$\sigma_0 + \check{T} \propto \prod_{k=1}^{2\ell_{\max}} (t + \alpha_k^*)(t + \alpha_k) + \prod_{k=1}^{2\ell_{\max}} (t - \beta_k^*)(t - \beta_k), \quad (\text{A13})$$

$$\sigma_0 - \check{T} \propto \prod_{k=1}^{2\ell_{\max}} (t - \alpha_k^*)(t - \alpha_k) + \prod_{k=1}^{2\ell_{\max}} (t + \beta_k^*)(t + \beta_k), \quad (\text{A14})$$

$$-\check{\Sigma} + \check{T} \propto \prod_{k=1}^{2\ell_{\max}} (t + \alpha_k^*)(t + \alpha_k) - \prod_{k=1}^{2\ell_{\max}} (t + \beta_k^*)(t + \beta_k), \quad (\text{A15})$$

$$-\check{\Sigma} - \check{T} \propto \prod_{k=1}^{2\ell_{\max}} (t - \alpha_k^*)(t - \alpha_k) - \prod_{k=1}^{2\ell_{\max}} (t - \beta_k^*)(t - \beta_k). \quad (\text{A16})$$

The problem is now to find out which kinds of discrete ambiguity transformations, when applied to the roots $\{\alpha_k, \beta_k\}$, leave the full set of quantities Eqs. (A11) to (A16) invariant, while also satisfying the multiplicative constraint Eq. (10).

The first set of transformations which comes to mind is given by the well-known double ambiguity:

$$\alpha_k \rightarrow \alpha_k^* \text{ and } \beta_k \rightarrow \beta_k^* \quad \forall k = 1, \dots, 2\ell_{\max}. \quad (\text{A17})$$

But other transformations may also be possible in addition, since the observable \check{P} is missing from the full diagonalizable set $\{\sigma_0, \check{\Sigma}, \check{T}, \check{P}\}$. Ideas that one would have to test are, for instance, exchange symmetries

$$\alpha_k \rightarrow \beta_k \text{ and } \beta_k \rightarrow \alpha_k \quad \forall k = 1, \dots, 2\ell_{\max}, \quad (\text{A18})$$

sign changes

$$\alpha_k \rightarrow -\alpha_k \text{ and } \beta_k \rightarrow -\beta_k \quad \forall k = 1, \dots, 2\ell_{\max}, \quad (\text{A19})$$

or combinations of both

$$\alpha_k \rightarrow -\alpha_k^* \text{ and } \beta_k \rightarrow -\beta_k^* \quad \forall k = 1, \dots, 2\ell_{\max}. \quad (\text{A20})$$

All of these ideas indeed do not violate the constraint Eq. (10). In case any such additional symmetry of the quantities Eqs. (A11) to (A16) were found, the next step would be to test which of the remaining three observables $\{F, G, E\}$ resolves the symmetry. Neither of the proposed symmetries Eqs. (A18) to (A20) leaves all the six quantities Eqs. (A11) to (A16) invariant. It remains to be asked whether such additional symmetries actually exist. In case they do not exist, the discussion would be simplified significantly [since \check{F} and \check{G} in this case already resolve the double ambiguity Eq. (A17)]. Due to information-theoretical reasons, it only seems permissible to simultaneously use three of the quantities from Eqs. (A11) to (A16), i.e., to use three new quantities obtained via invertible and linear transformations from the three diagonal initial observables $\{\sigma_0, \check{\Sigma}, \check{T}\}$.

As an example, one can select the three quantities given by Eqs. (A11) to (A13). The full set of discrete ambiguity-transformations, which, when applied to the roots $\{\alpha_k, \beta_k\}$, leaves Eqs. (A11) and (A12) invariant while maintaining the constraint in Eq. (10), is given by the two transformations in Eqs. (A17) and (A19). Under the exchange symmetry Eq. (A18), Eqs. (A11) and (A12) are transformed into each other and thus are not invariant.

Now considering additionally the quantity in Eq. (A13), one can see that while the transformation Eq. (A17) leaves this quantity invariant, transformation Eq. (A19) does not. This only leaves one possible conclusion, namely, that also for the case of only three diagonal observables $\{\sigma_0, \check{\Sigma}, \check{T}\}$, or equivalently the three new quantities in Eqs. (A11) and (A13), the double ambiguity is the only relevant discrete ambiguity of the problem.¹¹

The argument given above can be repeated for any other case where a combination of three quantities from the six definitions Eq. (A11) to (A16) is taken as a starting point.

¹¹This statement is of course only true in case transformations Eqs. (A17) and (A19) are indeed the only possible discrete ambiguities of the quantities in Eqs. (A11) and (A12) and that no further such discrete ambiguities exist. This seems plausible when considering equations Eqs. (A11) and (A12), in combination with the constraint in Eq. (10).

None of the other starting combinations is necessary for a proof, since this would give a redundant derivation, with the same outcome.

3. Completeness of the set $\{\sigma_0, \check{\Sigma}, \check{T}, \check{F}, \check{G}, \check{E}\}$

It has already been shown in Refs. [18,19] that the observables \check{F} and \check{G} change sign under the double-ambiguity transformation.

All the arguments made up to this point prove that the set $\{\sigma_0, \check{\Sigma}, \check{T}, \check{F}, \check{G}, \check{E}\}$ is free of discrete ambiguities in the TPWA. Assuming furthermore that this set of six observables has no continuous ambiguities, the set is complete.

APPENDIX B: COVERED PHASE SPACE OF THE DATA USED

The phase-space coverages of the polarization observable data used are illustrated in Fig. 3. For a detailed description of the data see Secs. IV and III. The vertical orange lines correspond to the energy bins of the statistically weakest polarization observable G and indicate by which amount the dataset of another observable has to be shifted to match these energies.

APPENDIX C: ON THE CORRELATION OF PROFILE FUNCTIONS

The correlation of two random variables X and Y can be calculated using the Pearson correlation coefficient defined as [44]

$$\text{Corr}(X, Y) = \frac{\text{Cov}(X, Y)}{\sqrt{\text{Var}[X]\text{Var}[Y]}}, \quad (\text{C1})$$

with their respective variances Var and the covariance Cov between the two random variables. Under the assumption that the dimensionless observables do not have any correlation with each other, the covariance of the unpolarized differential cross-section $\sigma_0(W, \theta)$ (denoted with X) and a profile function [denoted $Y' = XY$ because $\sigma_0(W, \theta)$ was used to calculate the profile function] is

$$\begin{aligned} \text{Cov}(X, Y') &= E[XXY] - E[X]E[XY] \\ &= (E[X^2] - E[X]^2)E[Y] \\ &= \text{Var}[X]E[Y]. \end{aligned} \quad (\text{C2})$$

And similarly for the covariance of one profile function (denoted as $Y' = XY$) to another (denoted $Z' = XZ$):

$$\begin{aligned} \text{Cov}(Y', Z') &= E[XYXZ] - E[XY]E[XZ] \\ &= (E[X^2] - E[X]^2)E[Y]E[Z] \\ &= \text{Var}[X]E[Y]E[Z]. \end{aligned} \quad (\text{C3})$$

Substituting Eqs. (C2) and (C3), respectively, into Eq. (C1) the correlation for both cases is

$$\text{Corr}(X, Y') = \sqrt{\frac{\text{Var}[X]}{\text{Var}[Y']}} E[Y], \quad (\text{C4})$$

$$\text{Corr}(Y', Z') = \frac{\text{Var}[X]}{\sqrt{\text{Var}[Y']\text{Var}[Z']}} E[Y]E[Z]. \quad (\text{C5})$$

APPENDIX D: UNDERLYING ASSUMPTIONS

An enormous strength of Bayesian statistics is its clarity about the underlying assumptions and how these evolve into the statistical model used. In general one has N data pairs $(y, x)_i$, where the two components can be distinguished as follows:

- (1) The random variables $\mathbf{y} = (y_1, \dots, y_N)$ follow a certain distribution. In this context, these correspond to the values of the profile functions of the polarization observables $\check{\Omega}^\alpha(W, \theta)$.
- (2) The explanatory variables [23] $\mathbf{x} = (x_1, \dots, x_N)$ do not belong to any probability distribution. In this context, these are the angular values $\cos(\theta_i)$ at which the y_i were measured.

The underlying distribution of \mathbf{y} is of utmost importance because it defines the shape of the likelihood function and, by association, the structure of the parameter space. It is therefore essential to examine the distribution from which \mathbf{y} originates and discuss the validity of the assumptions involved. Hereby, an understanding of the data acquisition as well as the subsequent analysis, to extract values for the polarization observables, is mandatory. For this reason, special emphasis is placed on their discussion within this paper.

The polarization observables used within this analysis originate from measurements at multiple experimental facilities: ELSA [5], MAMI [53], and GRAAL [54]. The measured quantities are count rates, corresponding to differential cross sections, from which then, one or multiple polarization observables can be extracted. The two most common methods are a ‘‘binned chi-square fit’’ and an ‘‘unbinned maximum-likelihood fit’’ [41]. For the first case, it is common to use an asymmetry of the form

$$A \propto \frac{N_1 - N_2}{N_1 + N_2}, \quad (\text{D1})$$

where N_1, N_2 are normalized count rates of reconstructed $\gamma p \rightarrow \eta p$ events for different polarization states [39,40]. This has the advantage that systematic effects, for example, from the reconstruction efficiency, cancel out.

Certainly, the distribution of this asymmetry is not explicitly addressed in any of the analyses concerning polarization observables which the authors have encountered up to this point. However, since the distribution of A determines the structure of the likelihood distribution, it is mandatory to study its proper form.

The count rates N_1, N_2 are Poisson-distributed random variables. If the expectation value, typically denoted as λ , is high enough, the distribution goes over to a Gaussian distribution. In the case of the data used here, this should be a good assumption.

The sum or difference of two independent Gaussian distributed random variables, as present in Eq. (D1), is again Gaussian distributed, which can be shown, for example, using characteristic functions.

However, the ratio of two, eventually correlated, Gaussian distributions $Z = X/Y$ is far more complicated. A general treatment can be found in Ref. [55]. Additionally a

closed-form expression is given in Eq. (G3), of Appendix G 1. Indeed, there exist Gaussian shapes for the asymmetry A in certain limits, but there exists also the possibility for a bimodal distribution [55]. Therefore, the shape of the asymmetry A has to be checked for the absence of a bimodal structure. To use χ^2 as likelihood function, the distribution should be well approximated by a Gaussian distribution. These checks can be performed by inserting the corresponding values for the expectation values (μ_x, μ_y) , standard deviations (σ_x, σ_y) and correlation (ρ) into the formula for Z and its transformation, see Ref. [55], or by using Eq. (G3).

An alternative approach, where the utilization of such an asymmetry can be circumvented, is the already mentioned ‘‘unbinned maximum-likelihood fit.’’ Albeit, in contrast with the first method, the detector acceptance has to be taken into account [41], which is possible [56]. Within this approach, the likelihood distribution can be modeled appropriately using Poisson distributions.

Summarizing, it is advantageous to use the unbinned maximum-likelihood fit for future analyses in order to extract values for the polarization observables.

However, the distribution of the extracted polarization observables not only depends on the shape of the used likelihood function but also implicitly on the method used to estimate the parameter uncertainties. Again, the distribution of the parameters is rarely explicitly discussed within papers such as the references cited in Table III. The error analysis of MINUIT uses by default the HESSE approach [57], which assumes an asymptotic approximation to a Gaussian distribution for the parameters under consideration. Thus, it is likely that the parameters were assumed to be Gaussian distributed. Another indication in the same direction is that all data used within the present analysis (cf. Table III) do have symmetric statistical uncertainties [38–42].

The profile functions $\check{\Omega}^\alpha$ are calculated by a product of random variables. However, even when these two random variables are independent and Gaussian distributed, the result is not always a Gaussian, only when one of the standard deviations is very small, see Ref. [19] or Appendix G 2. Fortunately, this is the case for σ_0 as it is the observable in $p\eta$ photoproduction with an unprecedented accuracy.

APPENDIX E: ANALYSIS STEPS

This section explains in detail the analysis steps in order to determine the complex multipole parameters using Bayesian inference.

The posterior, which was in all of the analyses explicitly multimodal, and the goal to analyze the structure of the mathematical ambiguities present a major challenge with respect to the sampling of the posterior distribution. On the one hand, posteriors with multiple modes connected by regions of low posterior density persuade the Markov chains to get stuck within a certain mode, unable to explore multiple ones [23]. This results in drastically¹² failing MCMC convergence diag-

¹²This behavior was to be expected since \hat{R} is a measure whether all chains have converged to the same distribution.

nostics, such as the potential-scale-reduction statistic \hat{R} . On the other hand, the number of possible modes increases exponentially with the truncation order ℓ_{\max} . An upper limit can be given by $2^{4\ell_{\max}} - 2$, as this is the maximal possible number of accidental ambiguities of the four group- \mathcal{S} observables [note that the bulk of this number is probably not realized as actual ambiguities due to the multiplicative constraint Eq. (10)] [19]. Capturing consistently all modes of the marginal posterior distributions via a large number of chains, with randomized starting values is computationally inefficient. Furthermore, randomized starting values will lead to traceplots where one cannot distinguish between chains that have not converged yet and chains which have explored more than one mode. An illustrative example is shown in Fig. 11.

These difficulties can be overcome by specifying well chosen starting values for the MCMC algorithm, explained in more detail in Appendixes E 2 and E 3. On that account, certain parts of the typical Bayesian workflow [58] had to be adapted.

1. Monte Carlo maximum *a posteriori* estimation

To compare between different solutions, found within the same analysis, it is important to find all modes of the marginal posterior distributions, especially the global maximum. As already mentioned, the number of accidental ambiguities rises exponentially with the truncation order. Thus, the utilization of an optimization routine is substantially more efficient¹³ than a large number of MCMC chains. With this in mind, a Monte Carlo maximum *a posteriori* estimation of the proposed posterior is employed as a preparatory step for the Bayesian inference procedure. The results of the following approach are cross-checked via an implementation in *Mathematica* [59], using the Levenberg-Marquard algorithm [60,61], as well as in Julia [62] using the L-BFGS-algorithm [63–67] via Optim.jl [68].

At first, one needs to fix the overall phase of the multipoles due to the bilinear product in Eq. (3). Indeed, without such a constraint the minimization algorithms would have convergence problems because the solutions are no longer located at isolated points in the parameter space but on continuous connected regions. Without loss of generality, a valid choice is $\text{Re}(E_{0+}) > 0$, $\text{Im}(E_{0+}) = 0$ [19]. Second, the minimization algorithm is performed for n different starting values. The starting values are chosen within the physically allowed parameter space, which solely depends on the total cross section σ_{tot} [19,69]. Fortunately, the unpolarized differential cross section is the most accurately measured observable in $p\eta$ photoproduction [1], thus yielding accurate limits. An appropriate amount of n equidistant points is chosen on each axis of this $(8\ell_{\max} - 1)$ -dimensional hyper-rectangle, such that the volume is sufficiently covered. Each of these parameter configurations is then used as starting values for the minimization algorithm.

Finally, the nonredundant solutions, of the n possible mode candidates can be extracted via a clustering algorithm. Hereby, all values of the multipole parameters are rounded

to six digits. Then the unique solution vectors can be filtered out. A rough estimate for the uncertainty of each parameter solution is calculated via the inverse of the Hesse matrix [70], i.e., assuming a Gaussian shape of the parameters.

2. Sampling of the posterior

Within this work, the well-established probabilistic programming software Stan [71] has been used to encode the model employed and to run the posterior sampling with the state-of-the-art Hamiltonian Monte Carlo algorithm [26,27] in combination with the No-U-Turn sampler [72]. The employed Stan model can be found in the Supplemental Material Ref. [49].

For each mode of the posterior distribution, determined within Sec. E 1, N_c chains are sampled with starting values for the multipole and systematic parameters equal to the corresponding $(8\ell_{\max} + 4)$ -dimensional solution vector. This approach ensures adequate sampling of all marginal posterior modes and enables again a meaningful convergence diagnostics, further discussed in Appendix E 3. Hence, this is true as long as the posterior modes are in the vicinity of the “typical set,”¹⁴ which is the case in this paper.

The following tuning parameters of the Hamiltonian Monte Carlo algorithm and the No-U-Turn sampler are adapted to the problem at hand. The average Metropolis acceptance probability $\delta \in [0, 1]$ is increased from its default value of 0.8 to $\delta = 0.99$. Thus, preferring a more fine-grained sampling, i.e., smaller leapfrog¹⁵ steps ϵ [72], over the additional computation time. The maximum tree depth, with a default value of 10, is increased to 50, so that the algorithm can explore even challenging posterior regions without hitting the termination conditions [71].

3. Monitor Markov chain Monte Carlo convergence

Naturally one is interested in how well the structure of the posterior was explored by the applied MCMC algorithm. The goal is to diagnose whether all Markov chains have explored the same part of the posterior distribution [23], i.e., whether the obtained distribution is reliable or accrued due to a random effect. This can be monitored by convergence diagnostics such as the potential-scale-reduction statistic \hat{R} [29] and Monte Carlo standard error [28] (which depends on the effective sample size [23]). Within this work, the adapted versions of these diagnostics, as proposed by Vehtari *et al.* [73], are employed. In addition, trace plots [30] can be used to monitor the behavior of chains which explore multiple marginal modes. For each of these diagnostics, it is essential to use multiple chains [30,73] for a reliable result.

However, a multimodal posterior provides some pitfalls. As already mentioned at the beginning of Appendix E, the Markov chains can get stuck in certain, isolated modes. Thus not all chains would have seen the same parts of the posterior

¹⁴An illustration of the typical set can be found in Ref. [50].

¹⁵This refers to one parameter of the leapfrog integrator; see, for example, Ref. [27].

¹³Integration is far more computation-intensive than differentiation.

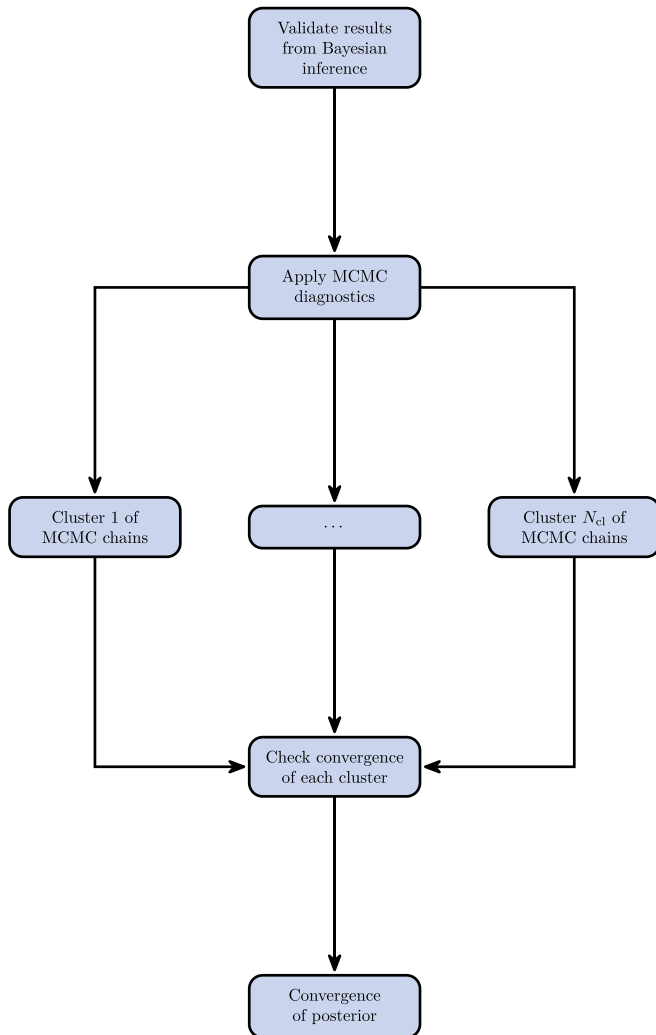


FIG. 13. Adapted workflow to monitor MCMC convergence due to a multimodal posterior.

distribution and the convergence diagnostics would indicate that the chains have not converged. Therefore, in case a multimodal posterior is studied, where all modes are of interest, the usual methods are not applicable. An adaptation has to be made. Under the assumption that all modes of the posterior were found via Monte Carlo maximum *a posteriori* estimation, see Appendix E 1, the following strategy is employed: A schematic representation of the adapted approach can be found in Fig. 13. Instead of applying the convergence diagnostics to all chains at once, the chains are clustered into groups according to their sampled parameter space and the convergence diagnostics are then applied onto each group separately.¹⁶ Consequently, the convergence for the whole posterior is monitored.

The chains can be grouped according to their similarity as follows: To avoid problems during the clustering process, coming from high-dimensional data [75], a dimensional reduction of the chains is performed. Each chain, consisting of

S sampling points, is characterized via a vector of its quantiles, in this case the [0.1, 0.2, 0.3, 0.4, 0.5, 0.6, 0.7, 0.8, 0.9] quantiles. Subsequently, the corresponding distance matrix [76] of the quantile vectors is calculated using the Euclidean metric. The constructed matrix serves as input for the Density-Based Spatial Clustering of Applications with Noise (DBSCAN) algorithm [77]. The minimal cluster size should be at least two, as this is the minimal amount of chains required to perform the \hat{R} diagnostic [30]. An appropriate ϵ neighborhood for the DBSCAN algorithm can be graphically determined, for example, by visualizing the Euclidean distances of the quantile vectors to each other. Afterwards, the correct clustering of chains can be checked visually. Alternatively, the two-sample Kolmogorov-Smirnov test [78] or the K -Sample Anderson-Darling test [79] could be employed to compare two distributions with each other.

The outlined approach still allows us to adjust the number of chains N_c per group and the sampling points S in order to gain adequate convergence diagnostics and the desired precision for the parameter estimates. Within this paper, one is aiming for $\hat{R} < 1.01$ [73] and a relative Monte Carlo standard error in the region of a few percent.

4. Analysis of generated data

It is crucial to prove the correct implementation and validity of the used model. An ideal testing scenario would be the *a priori* knowledge of the correct outcome of the analysis using the model under consideration. Therefore the PWA solution EtaMAID2018 [48] is employed for the electromagnetic multipoles in Eq. (4) up to the desired truncation order ℓ_{\max} . By these means, pseudodata for the profile functions $\hat{\Omega}^\alpha(W, \theta)$ are generated via Eq. (2) for certain energies and angular positions for the observables σ_0 , Σ , T , E , F , and G . These data were used as input for the TPWA following the described steps in Appendixes E 1 to E 3. This analysis yielded again the EtaMAID2018 multipole solutions, indicating a correct implementation.

APPENDIX F: CONVERGENCE DIAGNOSTICS

MCMC convergence diagnostics for the truncation orders $\ell_{\max} = 1$ and $\ell_{\max} = 2$ for all analyzed energies are shown in Figs. 10 and 6. The anticipated values for the potential-scale-reduction statistic $\hat{R} \leq 1.01$ and the relative Monte Carlo standard error (MCSE) of the median in the range of a few percent were achieved for both truncation orders. The diagnostics for 750 MeV are satisfactory, despite their slightly elevated values, which are the result of the highly multimodal marginal parameter distribution. However, certain convergence diagnostics for $\ell_{\max} = 2$ suggest that some groups of chains have not yet converged, indicating a specific phenomenon that will be discussed below. Hence, the four energies $E_\gamma^{\text{lab}} = [950, 1050, 1150, 1250]$ MeV look suspicious. In each case one group of chains show \hat{R} values way above 1.01 and relative Monte Carlo standard errors of over 100%. This results from two modes separated in phase space by a small region of low probability, so that the Metropolis acceptance probability [27] for a transition between the two high-probability regions

¹⁶A similar approach was used in Ref. [74].

is quite small but nonzero. Hence, just a small number of chains is able to explore both marginal modes at once, which is the reason for the suspicious convergence diagnostics. For the case of 1050 MeV, the blue distribution corresponds to a cluster with just one group member. Hence, it is not possible to calculate an \hat{R} value for this cluster. It is important to note that this behavior cannot be prevented because it is inherently a random effect. As an example how such a phenomenon manifests within a parameter distribution, see the blue distribution of $\text{Im}(M_{2+})$ at 1250 MeV in Fig. 8. Despite their convergence diagnostics, these types of distributions are shown within the multipole parameter and posterior predictive plots for their illustrative purposes.

APPENDIX G: PROBABILITY DISTRIBUTIONS FOR THE QUOTIENT AND PRODUCT OF TWO GAUSSIAN RANDOM VARIABLES

Assuming the original observables to follow a Gaussian probability distribution up to a very good approximation, the result of forming the quotient and/or product is generally non-Gaussian. This Appendix collects some basic facts about the quotient and the product distributions and considers some limiting cases.

1. The quotient distribution: $Z := X/Y$

Given are two independent, uncorrelated, Gaussian distributed random variables X and Y :

$$X \sim \mathcal{N}(\mu_X, \sigma_X), \quad Y \sim \mathcal{N}(\mu_Y, \sigma_Y), \quad (\text{G1})$$

together with the integral defining the probability distribution function of the quotient variable $Z := X/Y$ [80],

$$\begin{aligned} P_{X/Y}(u) &= \int_{-\infty}^{\infty} dx \int_{-\infty}^{\infty} dy \delta\left(\frac{x}{y} - u\right) \\ &\quad \times \frac{\exp\left[-\frac{1}{2}\left(\frac{(x-\mu_X)^2}{\sigma_X^2} + \frac{(y-\mu_Y)^2}{\sigma_Y^2}\right)\right]}{2\pi\sigma_X\sigma_Y} \\ &= \int_{-\infty}^{\infty} dy |y| \frac{\exp\left[-\frac{1}{2}\left(\frac{(uy-\mu_X)^2}{\sigma_X^2} + \frac{(y-\mu_Y)^2}{\sigma_Y^2}\right)\right]}{2\pi\sigma_X\sigma_Y}, \quad (\text{G2}) \end{aligned}$$

Mathematica yields the following result (for positive values of σ_X and σ_Y):

$$\begin{aligned} P_{X/Y}(u) &= f_1(u) \cdot \{\sqrt{2} f_2(u) c \\ &\quad + \sqrt{\pi} f_3(u) \text{erf}(f_4(u)) \exp[f_4(u)^2]\}, \quad (\text{G3}) \end{aligned}$$

with the declarations

$$f_1(u) := \frac{\exp\left[-\frac{1}{2}\left(\frac{\mu_X^2}{\sigma_X^2} + \frac{\mu_Y^2}{\sigma_Y^2}\right)\right]}{\sqrt{2\pi} f_2(u)^3}, \quad (\text{G4})$$

$$f_2(u) := \sqrt{\sigma_X^2 + \sigma_Y^2 u^2}, \quad (\text{G5})$$

$$f_3(u) := \mu_Y \sigma_X^2 + \mu_X \sigma_Y^2 u, \quad (\text{G6})$$

$$f_4(u) := \frac{f_3(u)}{\sqrt{2} f_2(u) c}, \quad (\text{G7})$$

$$c := \sigma_X \sigma_Y \quad (\text{G8})$$

and the error function ‘‘erf’’ [81]. In the following, two limiting cases for Eq. (G3) are analyzed: first, the vanishing of the expectation values (i.e., $\mu_X = \mu_Y = 0$):

$$P_{X/Y}(u) = \frac{\sigma_X \sigma_Y}{\pi(\sigma_X^2 + \sigma_Y^2 u^2)}. \quad (\text{G9})$$

This is a result which is known from earlier publications on the quotient distribution, for instance [82].

Second, considering also unit standard deviations (i.e., $\sigma_X = \sigma_Y = 1$) the result Eq. (G9) further simplifies to

$$P_{X/Y}(u) = \frac{1}{\pi(1 + u^2)}. \quad (\text{G10})$$

This is the well-known Cauchy distribution.

2. The product distribution: $Z := XY$

Similar to Eq. (G2) the probability-distribution function for the product of two independent, uncorrelated Gaussian distributed random variables can be written [83] as

$$\begin{aligned} P_{XY}(u) &= \int_{-\infty}^{\infty} dx \int_{-\infty}^{\infty} dy \delta(xy - u) \\ &\quad \times \frac{\exp\left[-\frac{1}{2}\left(\frac{(x-\mu_X)^2}{\sigma_X^2} + \frac{(y-\mu_Y)^2}{\sigma_Y^2}\right)\right]}{2\pi\sigma_X\sigma_Y}. \quad (\text{G11}) \end{aligned}$$

By introducing an integral-representation for the δ function

$$\delta(xy - u) = \int_{-\infty}^{+\infty} \frac{dk}{2\pi} e^{ik(xy-u)} = \int_{-\infty}^{+\infty} \frac{dk}{2\pi} e^{ikxy} e^{-iku}, \quad (\text{G12})$$

one can bring Eq. (G11) into the following form:

$$P_{XY}(u) = \int_{-\infty}^{+\infty} \frac{dk}{2\pi} e^{-iku} F_k[\mu_X, \sigma_X; \mu_Y, \sigma_Y], \quad (\text{G13})$$

where

$$\begin{aligned} F_k[\mu_X, \sigma_X; \mu_Y, \sigma_Y] &= \int_{-\infty}^{\infty} dx \int_{-\infty}^{\infty} dy e^{ikxy} \\ &\quad \times \frac{\exp\left[-\frac{1}{2}\left(\frac{(x-\mu_X)^2}{\sigma_X^2} + \frac{(y-\mu_Y)^2}{\sigma_Y^2}\right)\right]}{2\pi\sigma_X\sigma_Y}. \quad (\text{G14}) \end{aligned}$$

This characteristic function can be solved analytically:

$$\begin{aligned} &F_k[\mu_X, \sigma_X; \mu_Y, \sigma_Y] \\ &= \int_{-\infty}^{\infty} dy \exp\left[-\frac{1}{2}ky(k\sigma_X^2 y - 2i\mu_X)\right] \frac{\exp\left[-\frac{(y-\mu_Y)^2}{2\sigma_Y^2}\right]}{\sqrt{2\pi}\sigma_Y} \\ &= \frac{\exp\left[-\frac{k(k\mu_Y^2\sigma_X^2 + k\mu_X^2\sigma_Y^2 - 2i\mu_X\mu_Y)}{2+2k^2\sigma_X^2\sigma_Y^2}\right]}{\sqrt{1+k^2\sigma_X^2\sigma_Y^2}}. \quad (\text{G15}) \end{aligned}$$

The final result has the shape of a Fourier integral:

$$P_{XY}(u) = \int_{-\infty}^{+\infty} \frac{dk}{2\pi} \exp[-iku] \times \frac{\exp\left[-\frac{k(k\mu_Y^2\sigma_X^2 + k\mu_X^2\sigma_Y^2 - 2i\mu_X\mu_Y)}{2+2k^2\sigma_X^2\sigma_Y^2}\right]}{\sqrt{1+k^2\sigma_X^2\sigma_Y^2}}. \quad (\text{G16})$$

In analogy to the quotient distribution, the limiting case $\mu_X = \mu_Y = 0$ shall be analyzed. The Fourier coefficients become

$$F_k[0, \sigma_X; 0, \sigma_Y] = \frac{1}{\sqrt{1+k^2\sigma_X^2\sigma_Y^2}}. \quad (\text{G17})$$

The result for the product distribution can in this case be written with a modified Bessel function of the second kind $K_n(z)$:

$$P_{XY}(u) = \frac{K_0\left(\frac{|u|}{\sigma_X\sigma_Y}\right)}{\pi\sigma_X\sigma_Y}. \quad (\text{G18})$$

This is the analog of Eq. (G9) from the case of the quotient distribution. For unit standard deviations, Eq. (G18) becomes simply $K_0(|u|)/\pi$, which is the analog of Eq. (G10).

For the product distribution, especially one limiting case is of interest for this paper, namely, where the standard deviation of one random variable almost vanishes (i.e., $\sigma_Y \rightarrow 0$). The characteristic function becomes

$$\lim_{\sigma_Y \rightarrow 0} F_k = \exp\left(-\frac{k(k\mu_Y^2\sigma_X^2 - 2i\mu_X\mu_Y)}{2}\right). \quad (\text{G19})$$

Substituting Eq. (G19) into Eq. (G16) and solving the integral gives the result:

$$P_{XY}(u) = \frac{\exp\left(-\frac{(u-\mu_X\mu_Y)^2}{2\mu_Y^2\sigma_X^2}\right)}{\sqrt{2\pi}|\mu_Y||\sigma_X|}, \quad (\text{G20})$$

which is indeed a Gaussian probability distribution function. This result is used in Appendix D.

-
- [1] A. Thiel, F. Afzal, and Y. Wunderlich, Light Baryon spectroscopy, *Prog. Part. Nucl. Phys.* **125**, 103949 (2022).
- [2] R. L. Workman *et al.* (Particle Data Group), Review of particle physics, *Prog. Theor. Exp. Phys.* **2022**, 083C01 (2022).
- [3] R. Haensel, European synchrotron radiation facility, *Nucl. Instrum. Methods Phys. Res. Sect. A* **266**, 1 (1988).
- [4] T. Walcher, The Mainz microtron facility MAMI, *Prog. Part. Nucl. Phys.* **24**, 189 (1990).
- [5] W. Hillert, The Bonn electron stretcher accelerator ELSA: Past and future, in *Many Body Structure of Strongly Interacting Systems*, edited by H. Arenhövel, H. Backe, D. Drechsel, J. Friedrich, K.-H. Kaiser, and T. Walcher (Springer, Berlin, Heidelberg, 2006), pp. 139–148.
- [6] C. W. Leemann, D. R. Douglas, and G. A. Krafft, The continuous electron beam accelerator facility: CEBAF at the Jefferson laboratory, *Ann. Rev. Nucl. Part. Sci.* **51**, 413 (2001).
- [7] C. Yamanaka, Super photon ring-8 and its application to FEL, *Nucl. Instrum. Methods Phys. Res. Sect. A* **318**, 239 (1992).
- [8] R. A. Arndt, W. J. Briscoe, I. I. Strakovsky, and R. L. Workman, Extended partial-wave analysis of πn scattering data, *Phys. Rev. C* **74**, 045205 (2006).
- [9] A. Anisovich, R. Beck, E. Klempt, V. Nikonov, A. Sarantsev, and U. Thoma, Properties of baryon resonances from a multi-channel partial wave analysis, *Eur. Phys. J. A* **48**, 1 (2012).
- [10] D. Rönchen, M. Döring, and U.-G. Meißner, The impact of $K^+\Lambda$ photoproduction on the resonance spectrum, *Eur. Phys. J. A* **54**, 1 (2018).
- [11] D. Drechsel, O. Hanstein, S. Kamalov, and L. Tiator, A unitary isobar model for pion photo- and electroproduction on the proton up to 1 GeV, *Nucl. Phys. A* **645**, 145 (1999).
- [12] T. Sato and T.-S. H. Lee, Meson-exchange model for πN scattering and $\gamma N \rightarrow \pi N$ reaction, *Phys. Rev. C* **54**, 2660 (1996).
- [13] A. Švarc, M. Hadžimehmedović, H. Osmanović, J. Stahov, L. Tiator, and R. L. Workman, Introducing the Pietarinen expansion method into the single-channel pole extraction problem, *Phys. Rev. C* **88**, 035206 (2013).
- [14] A. Anisovich, R. Beck, M. Döring, M. Gottschall, J. Hartmann, V. Kashevarov, E. Klempt, U.-G. Meißner, V. Nikonov, M. Ostrick *et al.*, The impact of new polarization data from Bonn, Mainz and Jefferson laboratory on multipoles, *Eur. Phys. J. A* **52**, 284 (2016).
- [15] M. Ronniger and B. C. Metsch, Effects of a spin-flavour-dependent interaction on the baryon mass spectrum, *Eur. Phys. J. A* **47**, 162 (2011).
- [16] V. F. Grushin, Photoproduction of pions on low-energy protons: Complete experiments and multipole analysis, in *Photoproduction of Pions on Nucleons and Nuclei*, edited by A. A. Komar (Nova Science, New York, 1989), p. 1.
- [17] L. Tiator, Towards a model-independent partial wave analysis for pseudoscalar meson photoproduction, *AIP Conf. Proc.* **1432**, 162 (2012).
- [18] Y. Wunderlich, R. Beck, and L. Tiator, The complete-experiment problem of photoproduction of pseudoscalar mesons in a truncated partial-wave analysis, *Phys. Rev. C* **89**, 055203 (2014).
- [19] Y. Wunderlich, Ph.D. thesis, Rheinische Friedrich-Wilhelms-Universität Bonn, 2019 (unpublished).
- [20] Y. Wunderlich, F. Afzal, A. Thiel, and R. Beck, Determining the dominant partial wave contributions from angular distributions of single- and double-polarization observables in pseudoscalar meson photoproduction, *Eur. Phys. J. A* **53**, 86 (2017).
- [21] A. Omelaenko, Ambiguities of the multipole analysis of neutral-pion photoproduction from nucleons, *Sov. J. Nucl. Phys.* **34**, 406 (1981).
- [22] T. Bayes, LII. An essay towards solving a problem in the doctrine of chances. By the late Rev. Mr. Bayes, F. R. S. communicated by Mr. Price, in a letter to John Canton, A. M. F. R. S., *Philos. Trans. R. Soc.* **53**, 370 (1763).
- [23] A. Gelman, J. B. Carlin, H. S. Stern, D. B. Dunson, A. Vehtari, and D. B. Rubin, *Bayesian Data Analysis* (CRC Press, New York, 2013).
- [24] N. Metropolis, A. W. Rosenbluth, M. N. Rosenbluth, A. H. Teller, and E. Teller, Equation of state calculations by fast computing machines, *J. Chem. Phys.* **21**, 1087 (1953).

- [25] W. K. Hastings, Monte Carlo sampling methods using Markov chains and their applications, *Biometrika* **57**, 97 (1970).
- [26] S. Duane, A. Kennedy, B. J. Pendleton, and D. Roweth, Hybrid Monte Carlo, *Phys. Lett. B* **195**, 216 (1987).
- [27] R. M. Neal, *MCMC using Hamiltonian Dynamics*, in *Handbook of Markov Chain Monte Carlo*, 1st ed. (CRC Press, Boca Raton, 2011).
- [28] C. J. Geyer, Introduction to Markov chain Monte Carlo, in *Handbook of Markov Chain Monte Carlo*, 1st ed. (CRC Press, Boca Raton, 2011).
- [29] A. Gelman and D. B. Rubin, Inference from iterative simulation using multiple sequences, *Stat. Sci.* **7**, 457 (1992).
- [30] A. Gelman and K. Shirley, Inference from simulations and monitoring convergence, in *Handbook of Markov Chain Monte Carlo*, 1st ed. (CRC Press, Boca Raton, 2011).
- [31] A. M. Sandorfi, S. Hoblit, H. Kamano, and T.-S. H. Lee, Determining pseudoscalar meson photoproduction amplitudes from complete experiments, *J. Phys. G* **38**, 053001 (2011).
- [32] G. F. Chew, M. L. Goldberger, F. E. Low, and Y. Nambu, Relativistic dispersion relation approach to photomeson production, *Phys. Rev.* **106**, 1345 (1957).
- [33] W.-T. Chiang and F. Tabakin, Completeness rules for spin observables in pseudoscalar meson photoproduction, *Phys. Rev. C* **55**, 2054 (1997).
- [34] P. Kroenert, Y. Wunderlich, F. Afzal, and A. Thiel, Minimal complete sets for two-pseudoscalar-meson photoproduction, *Phys. Rev. C* **103**, 014607 (2021).
- [35] M. Pichowsky, Ç. Şavkli, and F. Tabakin, Polarization observables in vector meson photoproduction, *Phys. Rev. C* **53**, 593 (1996).
- [36] Y. Wunderlich, A. Švarc, R. L. Workman, L. Tiator, and R. Beck, Toward an understanding of discrete ambiguities in truncated partial-wave analyses, *Phys. Rev. C* **96**, 065202 (2017).
- [37] R. L. Workman, L. Tiator, Y. Wunderlich, M. Döring, and H. Haberzettl, Amplitude reconstruction from complete photoproduction experiments and truncated partial-wave expansions, *Phys. Rev. C* **95**, 015206 (2017).
- [38] V. L. Kashevarov, P. Ott, S. Prakhov, P. Adlarson, F. Afzal, Z. Ahmed, C. S. Akondi, J. R. M. Annand, H. J. Arends, R. Beck, A. Braghieri, W. J. Briscoe, F. Cividini, R. Codling, C. Collicott, S. Costanza, A. Denig, E. J. Downie, M. Dieterle, M. I. Ferretti Bondy, and L. Zana (A2 Collaboration at MAMI), Study of η and η' photoproduction at MAMI, *Phys. Rev. Lett.* **118**, 212001 (2017).
- [39] O. Bartalini, V. Bellini, J. Bocquet, P. Calvat, M. Capogni, L. Casano, M. Castoldi, A. d'Angelo, J.-P. Didelez, R. Di Salvo *et al.*, Measurement of η photoproduction on the proton from threshold to 1500 MeV, *Eur. Phys. J. A* **33**, 169 (2007).
- [40] C. S. Akondi, J. R. M. Annand, H. J. Arends, R. Beck, A. Bernstein, N. Borisov, A. Braghieri, W. J. Briscoe, S. Cherepnaya, C. Collicott, S. Costanza, E. J. Downie, M. Dieterle, A. Fix, L. V. Fil'kov, S. Garni, D. I. Glazier, W. Gradl, G. Gurevich, P. Hall Barrientos, and M. Wolfes (A2 Collaboration at MAMI), Measurement of the transverse target and beam-target asymmetries in η meson photoproduction at MAMI, *Phys. Rev. Lett.* **113**, 102001 (2014).
- [41] F. N. Afzal, Ph.D. thesis, Rheinische Friedrich-Wilhelms-Universität Bonn, 2019 (unpublished).
- [42] J. Müller, J. Hartmann, M. Grüner, F. Afzal, A. Anisovich, B. Bantes, D. Bayadilov, R. Beck, M. Becker, Y. Beloglazov, A. Berlin, M. Bichow, S. Böse, K.-T. Brinkmann, T. Challand, V. Crede, F. Dietz, M. Dieterle, P. Drexler, H. Dutz *et al.*, New data on $\bar{\gamma}p \rightarrow \eta p$ with polarized photons and protons and their implications for $N^* \rightarrow N\eta$ decays, *Phys. Lett. B* **803**, 135323 (2020).
- [43] F. Afzal *et al.* (A2 Collaboration) (unpublished).
- [44] E. W. Weisstein, Statistical correlation, From MathWorld—A Wolfram Web Resource. <https://mathworld.wolfram.com/StatisticalCorrelation.html>, accessed: 2022-05-30.
- [45] B. O'Neill, Exchangeability, correlation, and Bayes' effect, *Int. Stat. Rev.* **77**, 241 (2009).
- [46] M. Döring, J. Revier, D. Rönchen, and R. L. Workman, Correlations of πn partial waves for multireaction analyses, *Phys. Rev. C* **93**, 065205 (2016).
- [47] D. Rönchen, M. Döring, U.-G. Meißner, and C.-W. Shen, Light baryon resonances from a coupled-channel study including $K\Sigma$ photoproduction, *Eur. Phys. J. A* **58**, 229 (2022).
- [48] L. Tiator, M. Gorchtein, V. L. Kashevarov, K. Nikonov, M. Ostrick, M. Hadžimehmedović, R. Omerović, H. Osmanović, J. Stahov, and A. Švarc, Eta and etaprime photoproduction on the nucleon with the isobar model EtaMAID2018, *Eur. Phys. J. A* **54**, 210 (2018).
- [49] See Supplemental Material at <http://link.aps.org/supplemental/10.1103/PhysRevC.109.045206> for all parameter figures and the implementation of the used model within Stan.
- [50] M. Betancourt, A Conceptual Introduction to Hamiltonian Monte Carlo (2017).
- [51] R. L. Workman, R. A. Arndt, W. J. Briscoe, M. W. Paris, and I. I. Strakovsky, Parameterization dependence of t -matrix poles and eigenphases from a fit to πn elastic scattering data, *Phys. Rev. C* **86**, 035202 (2012).
- [52] A. Švarc and R. L. Workman, Laurent + Pietarinen partial-wave analysis, *Phys. Rev. C* **108**, 014615 (2023).
- [53] K.-H. Kaiser, K. Aulenbacher, O. Chubarov, M. Dehn, H. Euteneuer, F. Hagenbuck, R. Herr, A. Jankowiak, P. Jennewein, H.-J. Kreidel, U. Ludwig-Mertin, M. Negrazus, S. Ratschow, S. Schumann, M. Seidl, G. Stephan, and A. Thomas, The 1.5 GeV harmonic double-sided microtron at Mainz University, *Nucl. Instrum. Methods Phys. Res. Sect. A* **593**, 159 (2008).
- [54] O. Bartalini, V. Bellini, J. Bocquet, M. Capogni, L. Casano, M. Castoldi, P. Calvat, A. d'Angelo, R. Di Salvo, A. Fantini *et al.*, Measurement of π photoproduction on the proton from 550 to 1500 MeV at GRAAL, *Eur. Phys. J. A* **26**, 399 (2005).
- [55] G. Marsaglia, Ratios of normal variables, *J. Stat. Softw.* **16**, 1 (2006).
- [56] Jan Hartmann, Ph.D. thesis, Rheinische Friedrich-Wilhelms-Universität Bonn, 2017 (unpublished).
- [57] F. James and M. Roos, MINUIT: A system for function minimization and analysis of the parameter errors and correlations, *Comput. Phys. Commun.* **10**, 343 (1975).
- [58] A. Gelman, A. Vehtari, D. Simpson, C. C. Margossian, B. Carpenter, Y. Yao, L. Kennedy, J. Gabry, P.-C. Bürkner, and M. Modrák, Bayesian workflow, [arXiv:2011.01808](https://arxiv.org/abs/2011.01808).
- [59] W. R. Inc., Mathematica, Version 12.2 (2020), Champaign, IL.
- [60] K. Levenberg, A method for the solution of certain non-linear problems in least squares, *Q. Appl. Math.* **2**, 164 (1944).
- [61] D. W. Marquardt, An algorithm for least-squares estimation of nonlinear parameters, *J. Soc. Ind. Appl. Math.* **11**, 431 (1963).
- [62] J. Bezanson, A. Edelman, S. Karpinski, and V. B. Shah, Julia: A fresh approach to numerical computing, *SIAM Rev.* **59**, 65 (2017).

- [63] C. G. Broyden, The convergence of a class of double-rank minimization algorithms 1. General considerations, *IMA J. Appl. Math.* **6**, 76 (1970).
- [64] R. Fletcher, A new approach to variable metric algorithms, *Comput. J.* **13**, 317 (1970).
- [65] D. Goldfarb, A family of variable-metric methods derived by variational means, *Math. Comput.* **24**, 23 (1970).
- [66] D. F. Shanno, Conditioning of quasi-Newton methods for function minimization, *Math. Comput.* **24**, 647 (1970).
- [67] J. Nocedal, Updating quasi-Newton matrices with limited storage, *Math. Comput.* **35**, 773 (1980).
- [68] P. Mogensen and A. Riseth, Optim: A mathematical optimization package for Julia, *J. Open Source Software* **3**, 615 (2018).
- [69] D. Dreschsel and L. Tiator, Threshold pion photoproduction on nucleons, *J. Phys. G* **18**, 449 (1992).
- [70] R. J. Barlow, *Statistics: A Guide to the Use of Statistical Methods in the Physical Sciences* (John Wiley & Sons, 1993), Vol. 29.
- [71] S. D. Team, Stan modeling language users guide and reference manual, version 2.28, <https://mc-stan.org> (2022).
- [72] M. D. Hoffman and A. Gelman, The No-U-Turn sampler: Adaptively setting path lengths in Hamiltonian Monte Carlo, *J. Mach. Learn. Res.* **15**, 1593 (2014).
- [73] A. Vehtari, A. Gelman, D. Simpson, B. Carpenter, and P.-C. Bürkner, Rank-normalization, folding, and localization: An improved \hat{R} for assessing convergence of MCMC (with discussion), *Bayesian Anal.* **16**, 667 (2021).
- [74] Y.-C. Zhu, Z. Sun, and Q.-L. He, Clustering-based convergence diagnostic for multi-modal identification in parameter estimation of chromatography model with parallel MCMC, [arXiv:2107.07203](https://arxiv.org/abs/2107.07203).
- [75] K. B. Jonathan, J. Goldstein, R. Ramakrishnan, and U. Shaft, When is “nearest neighbor” meaningful? in *International Conference on Database Theory* (Springer, Berlin, Heidelberg, 1999), Vol. 1540, pp. 217–235.
- [76] R. L. Graham and H. O. Pollak, On the addressing problem for loop switching, *Bell Syst. Tech. J.* **50**, 2495 (1971).
- [77] M. Ester, H.-P. Kriegel, J. Sander, and X. Xu, A density-based algorithm for discovering clusters in large spatial databases with noise, in *KDD-96 Proceedings* (1996), Vol. 96, pp. 226–231.
- [78] Kolmogorov–Smirnov test, *The Concise Encyclopedia of Statistics* (Springer, New York, 2008), pp. 283–287.
- [79] F. W. Scholz and M. A. Stephens, K -sample Anderson-Darling tests, *J. Am. Stat. Assoc.* **82**, 918 (1987).
- [80] E. W. Weisstein, Normal ratio distribution, From MathWorld—A Wolfram Web Resource. <https://mathworld.wolfram.com/NormalRatioDistribution.html>, accessed: 2022-09-02.
- [81] E. W. Weisstein, Error function, From MathWorld—A Wolfram Web Resource. <https://mathworld.wolfram.com/Erf.html>, accessed: 2022-09-02.
- [82] J. H. Curtiss, On the distribution of the quotient of two chance variables, *Ann. Math. Stat.* **12**, 409 (1941).
- [83] E. W. Weisstein, Normal product distribution, From MathWorld—A Wolfram Web Resource. <https://mathworld.wolfram.com/NormalProductDistribution.html>, accessed: 2022-09-02.